Development of high-resolution multi-scale modelling system for simulation of coastal-fluvial urban flooding

Joanne Comer[1], Agnieszka Indiana Olbert[1], Stephen Nash[1], Michael Hartnett[1]

[1]Civil Engineering, College of Engineering and Informatics, Ryan Institute, National University of Ireland, Galway, University Road, Galway, Ireland

*Correspondence t*o: Dr. Agnieszka Indiana Olbert (indiana.olbert@nuigalway.ie)

Abstract. Urban developments in coastal zones are often exposed to natural hazards such as flooding. In this research, a state-of-the-art, multi-scale nested flood (MSN_Flood) model is applied to simulate complex coastal-fluvial urban flooding due to combined effects of tides, surges and river discharges. Cork City on Ireland's southwest coast is a study case. The flood modelling system comprises of a cascade of four dynamically linked models that resolve the hydrodynamics of Cork Harbour and/or its sub region at four scales 90m, 30m, 6m and 2m.

Results demonstrate that the internalisation of the nested boundary through a use of ghost cells combined with a tailored adaptive interpolation technique creates a highly dynamic moving boundary that permits flooding and drying of the nested boundary. This novel feature of MSN_Flood provides a high degree of choice regarding the location of the boundaries to the nested domain and therefore flexibility in model application. The nested MSN_Flood model through dynamic downscaling facilitates significant improvements in accuracy of model output without incurring the computational expense of high spatial resolution over the entire model domain. The urban flood model provides full characteristics of water levels and flow regimes necessary for flood hazard identification and flood risk assessment.

Keywords: Urban flooding; Coastal flooding; Fluvial flooding; Hydrodynamic modelling; Nesting; Moving boundary

1 Introduction

Low lying developments in coastal zones are exposed to natural hazards such as storm surges, waves, tsunamis and/or high river flows which can lead to significant flooding. Coastal flooding can result in substantial economic and social impacts including loss of life, damage to property and disruption of essential services (Brown et al., 2007).

Coastal flooding results from a rise of sea water level above normal predicted tide level. On the European Continental Shelf, coastal flooding is associated with storms generated in the Atlantic Ocean that travel through, or in proximity to, the shelf. Storm surges are important consequences of these storms – a temporary water setup resulting from synoptic variation of atmospheric pressure and strong winds blowing towards the shelf causing water to pile up against the coast. Surge physics is well understood in principle (Ponte, 1994); the mechanism of its propagation on the European continental shelf as a response to meteorological conditions (wind stress and atmospheric pressure signal separate) has been explained by Olbert and Hartnett (2010).

Flood dynamics due to a combination of multiple process drivers such as tides, surges and river inflows and their interactions is extremely difficult to understand using non-modelling methods (Robins et al., 2011). In recent years the amount of flood modelling work has risen dramatically. Yet the modelling still encounters various problems of which input data such as topography (Mason et al, 2007; Smith, 2002), mesh resolution (Sanders et al, 2010; Fewtrell, 2011; Horritt et al, 2006; Yu and Lane, 2006), bottom roughness (Mason et al., 2003; Horritt, 2000) or modelling framework (Hunter et al., 2008) are of greatest challenge. So far, one of the main issues hampering research into coastal flood modelling has been the lack of topographic data of sufficiently high resolution and accuracy along with highly resolvable efficient models. In the past decade, high resolution topographic has become more available with airborne scanning laser altimetry (LIDAR) technology (Gomes-Pereira and Wicherson, 1999) providing high resolution digital surface maps that can be used as model bathymetry (Marks and Bates, 2000). Although there are still problems with mapping urban areas and considerable post-processing is necessary to extract digital terrain model from digital surface model (Mason at al., 2007), the hydraulic/hydrodynamic models developed using LIDAR data allow them to numerically propagate surge and tidal waves into coastal areas. Model accuracy and computational cost are still issues to be addressed.

The most common and simple approach to the modelling of coastal flooding in urban areas is to link (externally or dynamically) longitudinal 1D or latterly averaged 2D hydraulic models with coastal models (e.g. Formaggia, 2001; Chen, 2007; Brown et al., 2007). Such a set up has two significant drawbacks. Firstly, 1D/2D hydraulic

59 models work with the assumption that the lateral variations in velocity magnitudes are small, while in reality

60 many coastal floodplains (e.g. urban areas) contain channels that have a significant influence on the

61 development of inundation by providing routes along which storm surges propagate inland (Bates et al., 2005)

62 and therefore may lead to misrepresentation of localized flooding (Cook and Merwade, 2009; Mark et al, 2004).

63 Secondly, numerical errors may be introduced when linking different models with different dimensions resulting

64 from poor conservation of momentum (Yang et al., 2012). There is evidence of proven difficulty in ensuring

65 that each model interprets the model inputs and boundary conditions in the same way (Hunter et al. 2008;

66 Pender and Neelz, 2010).

67 These problems may be overcome by application of a single hydrodynamic model to both coastal waters and

68 coastal floodplains. Although such a model would allow smooth transition of the model solution between

69 coastal waters and floodplains, the full solution at scales appropriate for flood inundation would incur a

70 significant computational cost. On one hand, such models need to extend far enough offshore to capture the

71 development and propagation of surge and to resolve the nonlinear shallow water dynamics (interactions

72 between tides, surges and waves) at a resolution that is commensurate with flow features. On the other hand the

73 model needs to include upstream river channels, tidal flats, low-lying land and urban areas which are susceptible

74 to flooding at very fine resolution. This often results in a model setup that requires a large computational domain

75 of which the area of particular interest (such as floodplains here) comprises only a small percentage. For

76 structured grid models such requirements are often cost prohibitive and the alternative is to use lower resolution

77 at the expense of accuracy. This means that model discretization is performed at scales well below those

78 achievable with LIDAR data (the level of individual buildings in the case of urban flooding) meaning the

79 highly-resolved LIDAR data are not being optimally used (McMillian and Brasington, 2007). Some quite

80 successful attempts have been made using unstructured-grid models allowing selective grid refinement (e.g.

81 Yang et al., 2012; Robins et al., 2011); however, the computational demand of these models is high. A relatively

82 new approach to address this problem in high-resolution flood modelling makes use of continuing advances in

83 computational resources through numerical domain decomposition and multi core architecture runs (Sanders et

84 al., 2010). This method, however, requires substantial computational resources not commonly available yet.

85 In reality the modelling of coastal flooding (particularly in an urban environment) is a multi-scale problem that

86 requires accurate solution at various scales ranging from coastal sea or estuary scale down to a dense street

87 network of the inundated urban area. In the case of single rectilinear grid models, which are still the most

88 commonly used hydrodynamic models, this spatial resolution problem may be overcome by grid nesting; this

89   involves embedding higher resolution grids within a lower resolution global large-scale grid model. Such a

90   solution allows users to specify high resolution in a sub-region of the model domain without incurring the

91   computational expense of fine resolution over the entire domain. Nonetheless, the nested model for simulation

92   of floodplains must be very carefully chosen due to the flooding and drying properties of such zones; most

93   nested models developed to date do not incorporate flooding and drying as they have been developed

94   specifically for large-scale application where this phenomenon is not important (e.g. ROMS, Haidvogel et al.,

95   2008) or, even if they incorporate flooding and drying such as Mike21 (DHI Software, 2001) flooding and

96   drying of open boundaries is prohibited. This problem has been recently resolved in the multi-scale nested flood

97   (MSN_Flood) model of Nash and Hartnett (2010) which allows flooding and drying both within the domain and

98   along boundaries, while maintaining accuracy and computational efficiency. This model is ideally suited for

99   high-resolution modelling of urban flooding and, therefore, has been adopted for further development in this

100   research.

101   In this context, the authors present in this paper for the first time the application of the state-of-the-art flood

102   model, MSN_Flood, to complex coastal-fluvial urban flooding in the estuary-lying Cork City which is subject to

103   the combined effects of tides, surges and river discharges. The primary objectives of this paper then are to

104   present the development of this model and to critically examine its capability to forecast/hindcast the urban

105   inundation. It will be demonstrated in this paper that through the novel solution to the nested boundary, the so-

106   called moving boundary, the nested model allows simulation of the propagation of open sea conditions up to the

107   tidally active river upstream as well as rural and urban floodplains in a computationally efficient manner without

108   compromising model accuracy or stability.

109   The modelling framework proposed in this research comprises of a cascade of multiple nested models that

110   dynamically downscale large scale, coastal sea processes to the fine resolution scale of urban environments.

111   MSN_Flood was applied to the area of Cork City, Ireland, and its coastal floodplains; Cork City is frequently

112   subject to coastal-fluvial flooding. An extreme flood event of November 2009 that resulted in approximately

113   €100 million of flood damage in the city and its surrounds was chosen as a test case. The main features of this

114   accurate and efficient hydraulic modelling are illustrated through the Cork City application. In particular,

115   wetting and drying routine, computational efficiency and accuracy of simulated water elevations and velocity

116   fields are subject to in-depth analysis in this research.

117   This paper is organized as follows: section 1 describes the motivation for this research and related work; section

118   2 describes modelling, model setup and datasets; section 3 presents and compares numerical model results with

119   observed datasets; section 4 discusses the advantages the MSN_Flood modelling system, and finally section 5

120   contains conclusions from the research.

121

122   **2 Methodology**

123   In this section a modelling system for coastal flood inundation is described along with the datasets and model

124   setup for the Cork City flood event.

125

126   **2.1 Modelling framework**

127   Many flood inundation events in urban environments have been modelled using simple hydraulic models, such

128   as HEC-RAS (Pappenberger et al., 2005) or LISFLOOD-FP (Bates and De Roo, 2000), incapable of simulating

129   flood water velocities required for accurate determination of flood wave propagation routes and assessment of

130   risks associated with a certain flood flow magnitude. A more realistic analysis can be achieved using a

131   hydrodynamic model that resolves both the continuity and momentum equations throughout the entire domain.

132   Here, the MSN_Flood model was applied to Cork City using a cascade of four nested grids to describe

133   hydrodynamics at various scales with particular interest in water elevations and velocity fields over the

134   inundated area. This nested model facilitates the refinement of spatial resolution in Cork Harbour from 90 m at

135   the outer reaches of the harbour down to 2 m in the streets of Cork City.

136

137   **2.2 Hydrodynamics**

138   MSN is a two-dimensional, depth-averaged, finite difference model and its solver is based on the alternate

139   direction implicit (ADI) solver developed by Falconer (1984) (Lin and Falconer, 1997; Nash and Hartnett,

140   2010). The governing differential equations used in the model to determine the water elevation and depth

141   integrated velocity fields in the horizontal plane are based on integrating the three-dimensional continuity and

142   Navier-Stokes equations over the water column depth. Assuming vertical accelerations are negligible compared

143   with gravity and that the Reynolds stresses in the vertical plane can be represented by a Boussinesq

144   approximation, then the depth integrated continuity and x-direction momentum equations are of the following

145   form (Falconer and Chen, 1991):

146

147

148

149   Continuity equation

$$\frac{\partial \zeta}{\partial t} + \frac{\partial q_x}{\partial x} + \frac{\partial q_y}{\partial y} = 0 \tag{1}$$

151

152   Momentum equation in x-direction

$$\frac{\partial q_x}{\partial t} + \beta \left[\frac{\partial U q_x}{\partial x} + \frac{\partial U q_y}{\partial y} \right] = f q_y - gH \frac{\partial \zeta}{\partial x} + \frac{\rho_a C^* W_x (W_x^2 + W_y^2)^{1/2}}{\rho} \tag{2}$$

154

$$- \frac{gU(U^2 + V^2)^{1/2}}{C^2} + 2 \frac{\partial}{\partial x} \left[\varepsilon H \frac{\partial U}{\partial x} \right] + \frac{\partial}{\partial y} \left[\varepsilon H \left[\frac{\partial U}{\partial y} + \frac{\partial V}{\partial x} \right] \right]$$

156   where, t = time

157   U,V = depth-averaged velocity components in the x,y directions

158   q_x, q_y = depth integrated volumetric flux components in the x,y directions ($q_x=UH$, $q_y=VH$)

159   H = total water depth

160   β = momentum correction factor for non-uniform vertical velocity profile

161   f = Coriolis parameter (= $2\omega Sin\ \phi$, where ω = angular velocity of the earth's rotation and ϕ =

162   geographical latitude)

163   g = gravitational acceleration

164   ρ_a, ρ = air and fluid densities respectively

165   C^* = air-water interfacial resistance coefficient

166   W_x, W_y = wind velocity components in x,y directions

167   C   = Chezy bed roughness coefficient

168   ε = depth mean eddy viscosity

169

170

171   **2.3 Nesting structure and procedure**

172   MSN_Flood consists of one outer coarse grid called the parent grid (PG) into which one or more inner fine grids

173   (child grids, CG) are one-way nested. The model also enables multiple nesting such that a child grid may also be

174   a parent to another child. In this way, multi-scale nesting can be specified enabling high spatial resolution in

175   areas of interest. PG and CG models are dynamically coupled and synchronous. An overview of the nesting

176   procedure is schematically presented in Fig. 1. As can be seen, the time integration is a bottom-up approach

177   where PG can be advanced in time only when all of its children are integrated to the parent current time. The

178   ADI solution technique to solve the governing continuity and momentum equations requires the sub-division of

179   each timestep into two half-timesteps. The nesting procedure, for each nesting level, is summarized in the

180   following 5 steps:

181   1. integrate outermost parent grid one timestep ($t+\Delta t_p$)

182   2. extract parent grid data and interpolate (spatially and temporally) along child grid boundary to next time

183   levels of child grid ($t+\frac{1}{2}\Delta t_c$) and ($t+\Delta t_c$)

184   3. integrate child grid one timestep ($t+\Delta t_c$)

185   4. repeat Steps 2 and 3 so that the child grid is synchronised to the current timestep of parent grid ($t+\Delta t_p$)

186   5. return to Step 1 and continue.

187   The nesting procedure is similar in principle to other nested models (Holt et al., 2009; Korres and Lascaratos,

188   2003; Nittis et al., 2006) but the uniqueness of MSN_Flood is a novel approach to boundary formulation

189   through an incorporation of ghost cells in a manner that the nested boundary operates as an internal boundary.

190   Ghost cells (GC) are specified adjacent to nested boundaries so that the boundary configuration consist of two

191   rows/columns of CG cells: internal boundary cells and the adjacent exterior ghost cells. A schematic of the

192   general configuration of the nested boundary is shown in Fig. 2. In this internal boundary approach, PG

193   boundary data is specified to both the ghost cells outside the CG domain and to the internal boundary cells

194   allowing the governing equations of motion at the internal boundary grid cells to be formulated and solved in

195   the same way as interior grid cells. This enables accurate specification and conservation of incoming fluxes of

196   mass and momentum along the boundaries of the nests. To demonstrate benefits of this approach the finite

197   difference formulation for the advective term in the momentum equation, which is key to momentum

198   conservation, at boundary cells becomes:

199

200
$$\frac{\partial Uq_x}{\partial x} = \left[\frac{[U(x+\Delta x, y)+U(x,y)]}{2} \cdot \frac{[q_x(x+\Delta x, y)+q_x(x,y)]}{2} \right. \tag{3}$$

201
$$\left. -\frac{[U(x,y)+U(x-\Delta x,y)]}{2} \cdot \frac{[q_x(x,y)+q_x(x-\Delta x,y)]}{2} \right]$$

202 For comparison, in a boundary formulation without ghost cells, the derivative $\partial U q_x / \partial x$ would be set to zero

203 as ghost cell grid points $U(x + \Delta x, y)$ or $U(x - \Delta x, y)$ would not exist, therefore momentum would not be

204 conserved between parent grid and child grid.

205 An important feature of the nesting approach in MSN_Flood is the implementation of moving boundaries along

206 the boundary of the nested domains. The flooding and drying routine originally developed in by Falconer and

207 Chen (1991) is implemented in MSN_Flood; this boundary formulation allows the model to be applied to areas

208 of inter-tidal zone or coastal flooding where there is typically a considerable degree of alternate flooding and

209 drying throughout the domain. The flooding and drying routine by Falconer and Chen has been extensively

210 tested in laboratory conditions and natural waterbodies and shown to be stable and robust. However, when the

211 nested boundary was subject to flooding and drying, despite the overall improvement in mass and momentum

212 conservation along the nested boundary, significant errors were found to occur near the boundary in areas of

213 flooding and drying. This problem was overcome by implementation of an adaptive interpolation scheme which

214 uses linear interpolation or zeroth-order interpolation depending on the status (wet or dry) and the configuration

215 of parent grids along the boundary interface. More details of the method can be found in Nash (2010). This

216 adaptive interpolation in combination with ghost cell and internal boundary formulation ensures the stable

217 flooding and drying of boundary cells.

218 The ghost cell formulation of the boundary was found to significantly reduce boundary formulation errors, one

219 of three error sources in nested models as classified by Nash and Hartnett (2010). Boundary formulation errors

220 arise from simplification of mathematical formulation of the governing equations of motion at open boundary

221 grid cells. Two other sources of errors at the boundary interface are boundary specification errors and boundary

222 operation errors. While the former errors arise from incorrect boundary data, and can be minimised by locating

223 nested boundary in areas of high PG accuracy, boundary operator errors result from the use of an inadequate

224 interpolation schemes and/or boundary condition for prescribing PG data to the CG boundary and are more

225 challenging to reduce. During the course of model developments various interpolation schemes were tested

226 including a zeroth order scheme, a linear scheme, a mass-conserving quadratic scheme and an inverse distance

227 weighted scheme. The linear interpolation was found to be most accurate in both time and space and therefore

228 was implemented in the model (Nash, 2010). With regards to the boundary conditions, three different types of

229 boundary conditions were tested, namely: Dirichlet condition, flow relaxation condition and radiation condition.

230 Extensive numerical testing showed that the most stable and accurate model solution could be achieved by

231   implementing the Dirichlet boundary condition. Accuracies of various interpolation and boundary condition

232   schemes were analysed and compared in Nash and Hartnett (2014).

233   Reduction in boundary errors due to the accurate development of boundary operators and more accurate

234   mathematical formulation of the nested boundary yielded significant improvements in conservation of mass and

235   momentum between parent and child grids. This in turn improved model stability at the nested boundary and

236   CG accuracy. These features make MSN_Flood highly applicable to modelling complex coastal flooding events

237   as in the current test case, where the nested boundary is located in the flooding and drying zone, and therefore

238   its length changes dynamically throughout the flooding event. This non-continuous moving boundary feature is

239   the subject of in-depth investigation in this research.

240

241

242   **2.4 Study area description and model setup**

243   Cork Harbour, in the southwest of Ireland, is a shallow (average depth 8.4 m) meso-tidal estuary with typical

244   spring tide ranges of 4.2m. Return levels of tides for 2- and 100-year return periods are 4.45 m and 4.52 m

245   above chart datum, respectively, while surge residual return levels for the same return periods are 0.56 m and

246   0.85 m, respectively (Olbert and Hartnett, 2013). The Cork Harbour domain is presented in Fig. 3. Cork City is a

247   densely populated urban area of approximately 120,000 people, located at the mouth of the River Lee which

248   drains into Cork Harbour. Tidal components of flooding in Cork City are due to combinations of high

249   astronomical tides and storm surges generated in the open ocean and propagating into the Harbour and

250   throughout the city streets. The River Lee corridor flows from west to east along the post-glacial valley into the

251   Lee proper, through Cork City, into Lough Mahon, Cork Harbour and south into Atlantic Ocean. In the city, the

252   River Lee bifurcates into the north and south channels around the Mardyke area and merges again at the eastern

253   edge of the city. The river flows for 2- and 100-year return periods are 208.6 and 307.7 m^3/s, respectively

254   (Halcrow, 2008). Sea water intrusion up the river is bounded by a weir located 8km upstream from the river

255   mouth.

256   MSN_Flood was used in this research to develop a coastal-urban hydraulic model capable of simulating fluvial

257   and coastal flooding in the Cork City. The model grid needs to be setup to include not only river channel and

258   urban floodplains but also offshore waters necessary to resolve the non-linear hydrodynamics. The Cork

259   Harbour/City model is therefore configured as a four level cascade of dynamically linked nested grids that

260   resolve the hydrodynamics of the region at spatial scales of 90m, 30m, 6m and 2m. Each coarser grid provides

261 boundary conditions to the next finer grid, i.e. the 90m grid provides boundary conditions to the30m grid and

262 the 30 m grid provides boundary conditions to the 6m grid, etc. Fig. 4a illustrates the extent of each grid and the

263 nesting structure, while Fig. 4b shows details of the high resolution 6m grid and the 2m urban flood grid.

264 The parent grid (PG90) representing the full domain of Cork Harbour was resolved at a grid spacing of 90m. At

265 3:1 nesting ratio, the first child grid (CG30), completely embedded within the parent model domain, has a grid

266 spacing of 30m. The CG30 model provides boundary conditions to a 6m grid (CG06) at a 5:1 nesting ratio. The

267 domains of CG30 and CG06 models only partially overlap. Water elevations computed on CG30 are passed to

268 the eastern boundary of CG06 while River Lee flow data are specified at the western boundary of CG06.

269 Finally, the ultra-high resolution 2m child grid (CG02) is entirely embedded within CG06 and is used to

270 simulate urban flooding of Cork City. The nesting ratios of 3:1 and 5:1 used in this setup are in line with nesting

271 ratios used in other studies (e.g. Spall and Holland, 1991). Configurations of the nested models are summarized

272 in Table 1.

273 Open boundary conditions to the MSN_Flood parent grid, PG90, are provided as total water elevations

274 containing tidal and surge signals extracted from an ocean model of the North East Atlantic (Olbert and

275 Hartnett, 2010). The surface boundary of the MSN_Flood model is forced by 10-m wind fields and mean sea

276 level atmospheric pressure obtained from the regional analysis ERA-40 model (Uppala et al., 2005) and

277 operational model first-guess dataset (Simmons et al., 1989). River Lee discharges from gauge station 19011

278 were provided by Office of Public Works (OPW), Ireland. Admiralty Chart data were used to develop the

279 bathymetric model of Cork Harbour, while high resolution LiDAR data provided by the OPW were used to

280 construct the high resolution urban digital bathymetric model. The channel of the River Lee was included in the

281 model based on cross-sectional survey data also provided by the OPW from an extensive survey of the River

282 Lee catchment in 2008.

283

284 **2.5 Verification**

285 The numerical model skill was assessed by statistically comparing observations and model solutions. Following

286 statistical measures were used:

287 • root mean square error

288 $$RMSE = \left[\frac{1}{N} \sum_{n=1}^{N} \left(Y_n - X_n \right)^2 \right]^{1/2}$$ (4)

289 • root mean square difference between model and observations

290 $$RMSdiff = \left[\frac{1}{N} \sum_{n=1}^{N} (Y_n)^2 \right]^{1/2} - \left[\frac{1}{N} \sum_{n=1}^{N} (X_n)^2 \right]^{1/2}$$ (5)

291 • centered root mean square difference

292 $$RMSD = \left[\frac{1}{N} \sum_{n=1}^{N} \left((Y_n - \overline{Y}) - (X_n - \overline{X}) \right)^2 \right]^{1/2}$$ (6)

293 where $\overline{X}$ and $\overline{Y}$ are the mean values of variables X and Y, respectively, for N observations. These

294 measures were also used to inter-compare time-series of models of different resolutions.

295 The spatially comparative measures between various models are based on spatial distribution of errors between

296 fine and coarse resolution models and are quantified using following expressions:

297 • tidally-averaged relative errors

298 $$RE_T = \frac{\sum_{n=1}^{N} |Y_n - X_n|}{\sum_{n=1}^{N} |X_n|} \cdot 100$$ (7)

299 • domain-averaged relative error

300 $$RE_D = \frac{RE_T}{M}$$ (8)

301 • absolute error

302 $$AE_T = \frac{\sum_{n=1}^{N} |Y_n - X_n|}{N}$$ (9)

303 • relative difference

304 $$RD = \frac{|X_n - Y_n|}{X_n}$$ (10)

305 where X and Y are higher and coarser resolution solutions, respectively, n is the output time over a tidal

306 cycle, $N=25$ is the total number of tidal cycles and M is the number of discrete points in space.

307

308 **3 Results**

309 Showcasing the capability of the multilevel nesting integrated system to accurately simulate the extent and level

310 of urban flooding is central to this research. MSN_Flood has been extensively tested in both laboratory settings

311   (against physical tidal models) and natural open harbours. In this research, a comprehensive validation of the

312   model in a coastal flood application to Cork Harbour and the urban environment of Cork City is presented.

313   Initial evaluation of model accuracy is carried out at each of the four levels of nesting; both modelled water

314   elevations and velocities are compared to available field data. The assessment of the model skill in simulation of

315   urban flooding is carried out for the November 2009 coastal-fluvial flooding of Cork City. In this application,

316   the city streets and open areas are treated as hydraulics channels and plains that can be inundated depending on

317   the tide, surge and fluvial conditions. This is a highly complex hydrodynamic region to model and, therefore,

318   represents a robust test of the model.

319

320

321   **3.1 Validation of the nesting procedure**

322   **3.1.1 PG90 model**

323   Firstly, the performance of the low resolution 90m parent grid (PG90) model was assessed. Figure 5 compares

324   current velocities simulated by the PG90 model with measured data at Passage West in Cork Harbour over a

325   spring tidal cycle (see Fig. 3 for point P1 location). Results show that although pattern of currents through flood

326   and ebb conditions are relatively well predicted, the slack water conditions, where velocities are generally

327   smaller, are not reproduced correctly by the PG90 model. A higher resolution single grid (SG30) model at 30m

328   grid spacing was developed to test the accuracy of PG90. The same domain extents (Fig. 4) and the same

329   physical conditions were specified to the SG30 and PG90 models. As shown in Fig. 5 an increased resolution of

330   the model significantly improves model predictions throughout the tidal cycle and particularly during periods of

331   slack water.

332   The spatial distribution of PG model error was quantified by calculating the tidally-averaged relative errors

333   RE_T expressing a percentage error in a PG solution relative to a higher resolution SG reference solution

334   (Equation 7). Figure 6 shows the distribution of RE_T in PG velocities in Cork Harbour; it can be seen that the

335   errors generated by the PG model are well over 30% at certain locations within the harbour (harbour entrance,

336   along the coastline, narrow channels and estuaries) so increasing the resolution from 90m to 30m leads to

337   significant reduction in the error. However, improvements in accuracy due to higher spatial resolution come at a

338   high computational cost which for the SG model (80min for 50hrs run) is nine times that of the PG model (9min

339   for 50 hrs run). The use of nested model is then a justifiable and favourable solution.

340 In the course of extensive validation, the timeseries of PG90 and SG30 were also inter-compared. Figure 7

341 shows water elevations and current velocities in Lough Mahon (see Fig. 3 for point C1 location). Water

342 elevations computed by both models are in very good agreement. In contrast, current velocities are significantly

343 overpredicted by the PG90 model. Linear regression of current speeds of PG90 against SG30 solution is shown

344 in Fig. 8. As can be seen from this figure the correlation coefficient between PG90 and SG30 is 0.89 while slope

345 and intercept are m=1.24 and c=0.03, respectively.

346

347 **3.1.2 CG30 model**

348 The selection of a child grid domain configuration is sensitive to the location of boundaries that may affect the

349 overall stability and performance of the nested model solution. Suitable CG boundaries must be located in areas

350 of low PG inaccuracy and at a sufficient distance from the area of interest as location of the boundary close to

351 the area of interest may result in boundary errors propagating into the area causing the accuracy of the solution

352 to deteriorate. On the other hand, boundaries need to be sufficiently close to the area of interest in order to

353 minimize the domain size (computational cost).

354 The first level child grid, CG30, was located in the north-west part of Cork Harbour with the centrally located

355 Lough Mahon (directly feeding to the River Lee estuary) being the area of interest. The boundaries for the CG30

356 domain were chosen based on the RE_T distribution plot for the PG90 current velocities presented in Fig. 6. The

357 upper section of Passage West, connecting Lough Mahon with Lower Harbour, was selected as a suitable

358 southern boundary (SB) due to its relatively low RE_T while the closest suitable location for the eastern

359 boundary (EB) was at a much greater distance from Lough Mahon due to generally high PG inaccuracies in the

360 North Channel.

361 The accuracy of the CG30 boundary location was assessed by comparing the net fluxes of mass and momentum

362 across the corresponding interfaces in the PG90, SG30 and CG30 models. Net fluxes were calculated normal to

363 boundaries. Mass and momentum fluxes through the SB and EB boundaries are compared in Fig. 9 and 10,

364 respectively. It can be seen that the predominant forcing-boundary for the CG30 domain is the SB boundary.

365 The tidally-averaged errors in PG90 fluxes relative to the SG30 were approximately 4% for both mass and

366 momentum indicating a high level of PG90 accuracy. At the EB boundary, the PG90 accuracy was slightly

367 lower resulting in error in PG90 mass flux of 5% and momentum flux of 10%. However, this boundary

368 accounted for a smaller portion of the total boundary forcing, and its distant location from the area of interest

369 allowed boundary errors more time to dissipate. The tidally-averaged errors in CG30 fluxes (both mass and

370 momentum) relative to PG90 fluxes were less that 2% at both boundaries, demonstrating high levels of

371 conservation from parent grid to child grid.

372 Relative error analysis was also carried out for the entire CG30 model domain with respect to water elevations

373 and velocities, and results of these analyses are summarized in Table 2. The domain-averaged relative error

374 (Equation 8) in the PG90 water elevations relative to the SG30 were 5.9% while in the CG30 model this error

375 was reduced to 1.1%. The extent of the domains with RE_T greater than 1% was 94% for PG90 and 28% for

376 CG30. The absolute error (Equation 9) was also calculated. AE_T in water level significantly decreased from

377 8cm in the PG90 to 1.2 cm in the CG30. In relation to current velocities, the RE_D was reduced from a large

378 value of 22.4% in PG90 to just 0.5% in CG30; while RE_T values exceeding 5% were found in 72% and 4% of

379 the PG90 and CG30 domains, respectively.

380 As shown in Fig. 7, timeseries of water elevations and current speed show very good agreement between SG30

381 and CG30 throughout the tidal cycle. This indicates significant improvement in the accuracy of velocity

382 computation using the high resolution nested CG30 and is verified by the linear regression analysis shown in

383 Fig. 8. The superiority of CG30 over PG90 model when compared to SG30 is clear and confirmed by a

384 correlation coefficient of 0.99 compared to 0.89. The slope and intercept were also improved for CG30 when

385 compared to PG90; with m=1.01 and c=-0.01 the CG30 against SG30 model solutions lie approximately on the

386 45° line.

387 These results demonstrate that the application of the nested high resolution model results in significant

388 improvement in the accuracy of the model solution over the lower resolution PG solution. Similar to the

389 improvement in model accuracy, an equally significant reduction in computational effort was achieved. For

390 example, the application of MSN_Flood model to level 1 domain nesting yields 21 minutes simulation time for

391 the PG90-CG30 model; this is contrasted by 80 minutes simulation time for the SG30 model. Thus the nested

392 model runs 3.8 times quicker than the single grid model.

393

394

395 **3.1.3 CG06 model**

396 In contrast to the CG30 grid being fully embedded within the PG90 grid, in the second level of nesting CG06 is

397 only partially nested within its parent CG30 (Fig. 4). Approximately 38% of wet cells in CG06 overlap CG30.

398 This is a hybrid boundary structure where the east boundary is prescribed using hydrodynamic data from the

399   parent model while the west boundary is prescribed using measured data. The west boundary is a flow

400   boundary, with River Lee inflows extracted from river gauging station 19011. The east boundary is a water

401   elevation boundary where water elevations are supplied along the boundary by the CG30 model. The location of

402   the latter boundary was selected to correspond to the position of the Tivoli tidal gauge station and therefore to

403   contribute to model validation (see Fig. 3 for location of Tivoli gauge).

404   Validation of the CG06 model is conducted for the flood event of November 2009, which due to a combination

405   of heavy river discharges and high tides coinciding with moderate surges resulted in extensive inundation of the

406   area delineated by this nested grid. Figure 11 compares timeseries of water elevation computed at the CG30-

407   CG06 nested boundary (east boundary) against tidal gauge records from the same location. Overall, there is a

408   very good agreement between predicted water elevations and measured data. The high degree of model accuracy

409   is manifested by high correlation (0.992) and a low value of RMSdiff (0.022m) shown in Table 3 (model

410   CG06_1). Both the RMSE (0.142m) and centred RMSD (0.141m) indicate that the model is able to reproduce

411   variability of water elevation with a good accuracy (order 0.14m). Further, a small difference between these two

412   statistical measures implies that the mean values of observations and simulation are very close. Interestingly, the

413   accuracy of the CG06 model is improved when a 6 minutes phase shift (one record timestep) between

414   observations and simulation is artificially introduced (model CG06_2 in Table 3). This results in RMSE

415   (RMSD) reduction to 0.106m (0.104m) and an increase of correlation to 0.996. It is deemed then that there is a

416   phase lag between model and observations of approximately one observational timestep. Another aspect of the

417   analysis involved temporal occurrence of an error. As the model-observations discrepancies are observed around

418   low water levels (which is not so significant to this study), by not considering negative water elevations (below

419   0 mOD Malin) the RMSE is further reduced to 0.075m (model CG06_3 in Table 3). Such level of agreement

420   between model and observation is considered to be satisfactory.

421   The effect of horizontal resolution on model skill is also examined. This is carried out by comparing the model

422   performance at 6 m and 2m resolutions. For this purpose a single grid 2m reference model (SG02) covering the

423   area delineated by the CG06 model was developed. Figure 12 presents the distribution of water level RE_T in

424   the CG06 solution relative to the SG02 reference solution. In general, errors in CG06 outside the Cork City

425   centre are very low (<10%) implying that flooding in the rural area of Cork is well resolved using the 6m grid.

426   In contrast, significantly higher errors are obtained in the Cork City (CG02 domain), and in particularly in areas

427   of narrow dense streets where errors exceed 30%. Here, an increase in model resolution leads to a significant

428 reduction in errors. This implies that next level of nesting is required to improve the model accuracy in the city

429 centre.

430

431 **3.1.4 CG02 model**

432 Finally, the highest resolution 2m model (CG02), fully embedded within CG06, covers the urban area of Cork

433 City; this area is particularly prone to flooding. In the first step of model skill analysis, water elevations

434 simulated by the CG06 and CG02 models at four locations along the river channel are compared in Fig. 13 and

435 statistically summarized in Table 4. Again, the November 2009 flood event was used as a benchmark. Close to

436 the east boundary, at point CG02_4 (see Fig. 14 for point location), both models perform almost identical and

437 this is visually and statistically confirmed in Fig. 13d and in Table 4, respectively. Discrepancies between the

438 CG06 and CG02 models increase with distance from the nested east boundary and are manifested by overall

439 higher water elevations computed by the coarser CG06 model. Location CG02_2 (Fig. 13b) shows the biggest

440 discrepancy evidenced by the statistical measures RMSE=0.195m, RMSD=0.109m, RMSdiff=-0.181m. Despite

441 overprediction of water elevations by the CG06 model, the general water level trends in the two models are in

442 good agreement (COR=0.997). Another important advantage of a high resolution model is an improved

443 numerical stability of the model solution. As can be seen from Fig. 13 a-c, some infrequent random oscillations

444 in water levels occurring in CG06 from numerical instability due to insufficient grid resolution are not present in

445 the finer CG02 model.

446 The numerical instability of the MSN_Flood model is directly related to the grid resolution and results from an

447 alternating direction implicit (ADI) algorithm used in the model's solution procedure. In general, the models

448 using ADI are very accurate numerically in modelling flows, however, in the presence of a discontinuity, such

449 as in regions of sharp gradients (e.g. velocity gradients, elevation gradient or high elevations), the numerical

450 models using such schemes are prone to generate spurious numerical oscillations (Kvočka et al., 2015). A

451 common solution used to reduce these oscillations is to increase the grid resolution so the slopes over numerical

452 grids are milder. Comparing time series outputs from CG06 and CG02 (Fig. 13), it is evident that increasing

453 resolution of the model significantly reduces numerical errors and hence oscillations.

454 The effect of improved horizontal resolution is analysed spatially by means of RE_T distribution plots. As

455 shown in Fig. 12, the 2m resolution is essential to resolve small scale processes of complex urban area. Figure

456 14 compares RE_T between CG02 and SG02. In general, RE_T is quite low at 10% in the western part of the

457 city along river banks increasing in eastward direction to 20% in narrow streets of city centre. This is a

458   considerable improvement when compared to RE_T in CG06 relative to SG02. Moreover, as CG02 achieves a

459   similar level of accuracy to SG02 the computational cost is significantly reduced and constitutes enormous 96%

460   saving.

461   From this analysis it can be seen that the CG06-CG02 nesting results in a model performance generally

462   comparable to the single grid SG02 model but at a significantly reduced computational cost when compared to

463   the single grid model.

464   The ultimate conclusion from the model validation is that MSN_Flood facilitates significant improvements in

465   model accuracy without incurring the computational expense of high spatial resolution over the entire model

466   domain. The model setup constitutes a rigorous test of model performance and on that basis it can be further

467   concluded that the model is applicable to situations where nested boundaries are located in complex urban

468   floodplains that periodically wet and dry.

469

470   **3.2 Urban flood modelling**

471   For most of the time, city streets are dry and rivers draining the hinterland are contained within well-defined

472   river banks or walls. However, when extreme flood events occur rivers may burst their banks and the city

473   streets become water conveyance channels. The simulation of the hydrodynamics associated with rapid urban

474   flood events is complex; many significant issues must be addressed such as flooding and drying, spatial

475   resolution, domain definition, frictional resistance and boundary descriptions. When modelling flood events, the

476   mathematical formulation of the nested boundaries that permit flooding and drying is of particular importance.

477   Also, the horizontal resolution necessary to resolve small scale processes must be considered. In particular,

478   these aspects of the MSN_Flood model will be discussed in this section.

479

480   **3.2.1 Extreme flood event**

481   On the 19th and 20th of November 2009 high River Lee flows combined with high astronomical tides and

482   moderate surge caused localized overtopping/breaching of the river banks resulting in widespread flooding of

483   Cork City. Evolution of the flood wave propagation simulated by the CG02 model is shown in Fig. 15.

484   Maximum flooding was reached at 9:30 on 20/11/2009 around the time of high tide and approximately 5 hours

485   after peak discharge of River Lee. At this juncture over 62ha of Cork City had been flooded. The most affected

486   zone was the city centre located between the north and south channels of the river; this area is a low-lying island

487   that over centuries was gradually reclaimed from marshland and it's low-lying topography combined with the

488   influence of river, estuary and harbour makes the area particularly vulnerable to flooding.

489   The accuracy of the urban inundation simulation was assessed against field observations of inundation extent

490   and maximum heights of flood waters. The observed and modelled ultimate extents of flooding in the city are

491   shown in the Fig. 16; the hindcasted extent of inundation matches very well that observed during the flood

492   event. With regards to flood level heights, observed water level marks were collected and post-processed by

493   OPW at 38 survey points across the flooded area; their distribution is shown in Fig. 17. The survey point data

494   were subsequently used to calibrate the model. Initial calibration tests showed that the model was most sensitive

495   to bottom roughness coefficient. An extensive statistical analysis of bed roughness parameterization was used to

496   provide an accurate model solution for flood inundation. The best fitting results (R=0.97, RMSD=0.26) were

497   obtained for the following roughness values: upper channel=0.90, lower channel=0.90, roads=0.1, city

498   floodplain=0.1 and upstream floodplain=0.30. Figure 18 provides visual assessment of the best fit model skill;

499   good agreement between the model and observations is achieved as the model solution falls on the 45° line.

500   Interestingly, better agreement was found for survey locations in floodplains as opposed to points adjacent to the

501   river bank. This could be attributed to the fact that the majority of survey points are located away from the

502   channel edge (many are actually at the floodplain edge).

503

3.3 Moving boundary

504

505   The specification of a nested boundary in a flood-prone area is particularly problematic; nested models

506   developed so far prohibit flooding and drying along open boundaries. This problem has been overcome in

507   MSN_Flood; its unique mathematical formulation of the nested boundary involving ghost cells, internal

508   boundary formulation and adaptive interpolation, ensures stable flooding and drying of boundary cells. In

509   MSN_Flood, any nested boundary can be placed within a flooding and drying zone and therefore may be subject

510   to significant lateral expansion and contraction. Moreover, the internalization of the boundary allows the

511   flooding and drying mechanism to approach the boundary of the nested domain from either upstream or

512   downstream. As the boundary alternatively floods or dries, the number of active boundary cells expands and

513   contracts accordingly. Depending on local topography, not only the length of the boundary may change but also

514   the number of active boundaries changes. Such a boundary is therefore a complex, non-continuous, moving

515   boundary that spatially and temporally changes its characteristics. This is a significant aspect of this research.

516   In the model setup, the urban CG02 model is entirely embedded within the CG06 model; mass and momentum

517   from the 6m model is transferred to the 2 m model via two nested boundaries – the western boundary

518   transferring River Lee waters from the upper to the lower channel of the river (it also geographically divides the

519   floodplains into upper and lower floodplains), and the eastern boundary exchanging waters with the estuary. The

520   western boundary of CG02 is located on the upstream fluvial floodplain which is prone to wetting and drying. A

521   cross section through this boundary illustrating the steep gradients of the river channel bathymetry and the

522   topography of the adjacent urban floodplains (which includes buildings) is shown in Fig. 19. The temporal

523   progression of water levels throughout the November 2009 flooding is also plotted. The reference water level at

524   simulation time t=4hr corresponds to a 187 m^3/s river flow (19th of November 2009 at 01:30). At this juncture

525   the flow greatly exceeds the average river flow of 40 m^3/s as it results from increased discharges from Inniscarra

526   dam. The storage capacity of Inniscarra Reservoir had been reached after a month-long period of record high

527   rainfalls and heavy downpours on the 18th and 19th of November. Over the course of the subsequent 28 hours

528   the discharges further increased to reach a maximum value of 560 m^3/s at 2:30 on November 20th. The water

529   level at the boundary increased from 4.57 mOD at 22:30 November 18th to a peak of 5.74 mOD 28 hours later.

530   The extensive inundation of the upper channel floodplains (upstream floodplains) has a major effect on the

531   western boundary of the CG02 model. It can be seen in Fig. 19 that as the flooding progresses to a simulation

532   time of 8hrs a second wetted boundary is created south of the main channel boundary due to bifurcation of

533   flood waters into two channels (called here the main and side channels) approximately 1.2km upstream of the

534   boundary. Importantly, there is a significant difference in water elevation of 0.41m between the two channels of

535   the boundary. This results from the topography of the upstream floodplains and therefore local flow conditions.

536   The reason for the difference in water elevations along the two sections of the boundary can be explained with

537   the help of Fig. 20 showing three cross-sections including one (cross-section 3) located close to the nested

538   western boundary. As simulated by the CG06 model, downstream from cross-section 1, representing the

539   maximum cross-sectional extent of the inundated area, flood waters must flow around an elevated strip of rural

540   land and so splits at this point into two floodplain channels. This is shown in cross-section 2, located at mid

541   length of this 1 km long strip of land; here the water elevation difference between two channels is 0.31m. This

542   elevation difference further increases to 0.41m near the nested boundary (cross-section 3).

543   The temporal rise of water levels at a number of points across the western nested boundary is shown in Fig. 21.

544   Series A represents the main river channel, series B and C correspond to points adjacent to the river channel

545 while series D is located in the side channel. The difference in water elevations between the two boundaries is

546 apparent throughout the entire flooding period, though it is reduced with the progress of flooding.

547 An interesting characteristics of the moving boundary is it change in its length. As flood waters continue

548 overtopping the river banks, the area of inundation increases and is reflected in the elongation of the boundary.

549 The length of the main channel boundary is initially equal to the river width, this nearly doubles during flooding

550 as shown for t=12 hrs in Fig. 19. The temporal evolution of flooding through the boundary clearly demonstrates

551 that the nested boundary is a discontinuous moving boundary with a variable head.

552 The numerical stability of such dynamically changing properties of nested boundary is an important aspect of

553 nesting procedures. Overall, a change in length as well as division into separate subsections does not markedly

554 impact computational stability nor model performance. In fact, as shown in Fig. 14, RE_T computed over the

555 flooding period remain low within the CG02 domain despite significant changes to nested boundary

556 configurations and flow conditions.

557 As demonstrated in this section MSN_Flood is developed in a general-purpose manner that through stable and

558 accurate moving boundary provides a high degree of choice and flexibility regarding the location of the

559 boundaries to the nested domain.

560

561 **3.4 Model resolution**

562 Due to the highly irregular topography of urban environments and the highly dynamic flows involved, urban

563 flooding is a complex problem. Most of the flood models developed so far have focused on rural or semi

564 developed floodplains where isolated large structures can be modelled while small objects are ignored or

565 parameterized as bottom friction (Brown et al., 2007). Such modelling does not implicitly account for locking

566 effects of building on flow. As the presence of buildings may substantially increase flood extent when compared

567 with undeveloped floodplains the role of high resolution discretization is paramount. However, as Brown et al.,

568 (2007) found, the greatest source of modelling error with respect to grid resolution is associated with the

569 steepest gradients in topography which are susceptible to interpolation error.

570 Modelling of flood flow through urban area is difficult because of its need for stable and accurate solution of the

571 flow equation (Brown et al., 2007). Since accurate modelling requires a resolution commensurate with flow

572 features, dense street network flows through urban floodplains can only be fully resolved with a sufficiently

573 high resolution. However, satisfactory model resolution, and thus accuracy, incurs computational expense; a

574 balance between these two contradicting factors provides an optimal solution. Gallegos et al. (2009) found that a

575 5m resolution mesh that spans a street by approximately three cells achieves such balance. The characteristics of

576 urban residential areas of southern Californian investigated in their study is different than that of an old

577 European development type towns comprising of narrow dense streets as Cork City. It follows that the 5m

578 model resolution is insufficient to resolve flow dynamics in such city centre street networks.

579 In order to analyse the overall effect of model resolution on simulation results, CG06 and CG02 model results

580 are compared. Visual comparison of flood inundation can be made from Fig. 22 which shows CG06 and CG02

581 model outputs representing the maximum extent of inundation during the November 2009 flooding. There is a

582 discrepancy in the extent and magnitude of flooding between the two models. Some zones and streets do not get

583 flooded in the CG06 model, which may be caused by the coarse representation of the street network and

584 associated lack of connectivity between certain streets, while in other zones flood water is present in areas

585 which remain dry according to observations and CG02 output. Figure 23 (a) shows the difference in water

586 elevations between CG02 and CG06 interpolated onto the 2m grid. It is clear that both the height and area of

587 flooding are affected. The absolute difference in water level is on average 0.13m and is underestimated by the

588 6m model by up to 0.4m in the upper section of river and overestimated by approximately 0.3m in the lower

589 section. Figure 23 (b) shows a spatial distribution of RMSE between two models. There is a noticeable reduction

590 in model performance at coarser resolution of 0.08m RMSE over the entire domain and the error is generally

591 larger in the dense street network of the urbanized zone. Based on model results it is clear that a substantial

592 portion of the error results from the coarse representation of topography since its gradient is greater that the

593 slope in water surface; however, some small portion of the error could be attributed to errors in LIDAR data

594 (~0.1m RMSE according to Bates et al, 2010) as well as interpolation from 6m down to 2m grid.

595 Another comparative measure involves a computation of relative differences (Equation 10) in inundated area

596 and flood water volume between fine and coarse grid models at a particular time. Figures 24 (a) and (b) show

597 the evolution of differences between CG02 and CG06 solutions in inundated areas and volumes throughout the

598 simulation. The significantly high relative difference in the area at the initial stage of flooding reaching 36% is

599 misleading as the relatively small total inundated area with a small flood time lag results in large discrepancies

600 at this stage (ca. 11ha). Nevertheless, when the flooding is more pronounced (over 30 ha, max 62.6ha) the

601 relative difference is still up to 10%. With regards to flood water volume in inundated areas the difference is

602 over 20% during first hours of flooding and still remains as high as 10% throughout the flood peak only falling

603   to below 10% when the flood recedes. The total RMSE of inundated area and volume between 2m and 6m

604   models are 3.4ha and 21,367m^3. This comparison demonstrates that horizontal resolution is of paramount

605   importance when simulating flows through complex topography. It seems that for Cork City centre comprising

606   of dense network of narrow streets, neither the 5m resolution requirement nor 3 cell street span would resolve

607   complex flood flow at satisfactory level of accuracy.

608

609   **3.5 Flood water velocities**

610   Another significant advantage of MSN_Flood is its ability to simulate the velocities of flood waters. As opposed

611   to simplified 2D hydraulic models frequently used in urban flooding, the hydrodynamic MSN_Flood includes

612   both the continuity and momentum equations, solving for both water elevations and water velocities. Figure 25

613   shows an example of flood water velocities computed by MSN_Flood in a selected area of Cork city centre

614   blown up for ease of viewing; one can see flood waters in both the river channel and the urban floodplain. This

615   zone is characterized by fast flowing shallow water subject to rapid transitions as it flows down through the

616   steep section of recreational grounds adjacent to the river channel. The city downtown, in contrast, is a ponding

617   area with relatively stagnant waters.

618   Knowledge of velocity fields facilitates better understanding of flood water hydrodynamics and in particular the

619   mechanisms of flood propagation. The routes and speeds of flood waves provide important information for the

620   evaluation of flood risks to people's safety and to property, as well as to the planning and actions of emergency

621   response teams.

622

623   **4 Discussion**

624   Inundation of coastal areas due to coastal and/or fluvial urban flooding mechanisms is a very complex

625   hydrological phenomena, and developing a modelling system to accurately simulate it is not a trivial task. The

626   research presented in this paper demonstrates that the concept of nesting models is very suitable for complex

627   urban coastal flooding as they facilitate the development of an integrated system capable of resolving

628   hydrodynamics at spatial scales commensurate with flows and physical features of the region of interest. The

629   modelling system adopted here determines physical processes simultaneously at different scales ranging from

630   bay-size circulation (90 m) through mesoscale processes of coastal waters at 30 m resolution down to the ultra-

631   high scale environment of 2m. Validation results show that the model performs well at each of these scales.

632 The MSN_Flood model developed for use in this research is well suited for high resolution urban flood

633 simulation for a number of reasons. Firstly, it allows smooth transition of the model solution between coastal

634 waters and river floodplains while giving a very high level of conservation of mass and momentum between

635 parent and child grid (Nash and Hartnett, 2010). Through incorporation of ghost cells and formulation of a

636 dynamic internal boundary, MSN_Flood is designed to minimize boundary formulation error and therefore to

637 transfer mass and momentum across the nested boundary without loss of nested solution accuracy. The

638 reduction in boundary errors yields also a significant improvement in model stability at the nested boundary and

639 CG accuracy. This in turn permits stable flooding and drying at the boundary; moreover, these process are

640 allowed to approach the boundary of the nested domain from either upstream or downstream. The so-called

641 moving boundary allows then embedding of a child grid model within the parent model in areas where the

642 nested boundary may wet or dry making the model highly flexible in application. Interestingly, such highly

643 reduced boundary formulation errors is achieved in a nesting mechanism where the nested boundary comprises

644 of only two cells of columns or rows (ghost cells and internal boundary cells). For comparison, in many nested

645 models poor accuracy due to boundary formulation errors is commonly compensated by indirect solutions such

646 as boundary configuration (e.g. location). For example, Kashefipour et al. (2002) in order to reduce possible

647 nesting error dynamically link 2D coastal model with 1D river model by using overlapping grids at the

648 boundary – a common area where boundary values are exchanged between two models. Such model setup is

649 not required in MSN_Flood where accurate exchange of boundary conditions occurs along a boundary.

650 Secondly, the model has virtually no limit to the number of specified nesting levels (and spatial resolution) and

651 is primarily constrained by computational effort rather than numerical stability. The highest resolution of 2 m set

652 for this study was dictated solely by the resolution of available LiDAR data and higher resolutions are easily

653 achievable if suitable terrain data is available. For example, a 0.025 m resolution was used to simulate flows

654 corresponding to those in a physical scale model of a harbour of dimensions 1.0x1.0x0.25 m (Nash and Hartnett

655 2014). In this way, the model allows improved accuracy of solution when compared to a lower resolution parent

656 model where the improved accuracy is similar to that of a similar high resolution single grid model but the

657 computational effort is significantly reduced.

658 Thirdly, the model provides adequate solutions at scales sufficient for processes of interest, such as coarse

659 resolution coastal circulation and fine resolution flood inundation. This is attributed to the robust hydrodynamic

660 module which in essence adopts the well-tested numerical scheme and discretisation methods described by

661 Falconer and Chen (1991). The uniqueness and improvement of MSN_Flood over other nested models is its

662 formulation of the nested boundary in the area where flooding and drying may occur. In order to accommodate

663 flooding and drying of boundary cells the model allows a moving nested boundary so that large sections of the

664 boundary can alternatively wet and dry. The stable flooding and drying of boundary cells results from the

665 internalisation of the nested boundary combined with an adaptive interpolation technique tailored specifically

666 for this model. To the author's knowledge the development of a non-continuous moving nested boundary in a

667 circulation model is novel. Such an innovative solution does not pose restrictions on the location of nested grids

668 with regards wetting and drying (as demonstrated by the application to Cork Harbour) and, therefore, allows

669 flexibility of model setup.

670 Finally, in the context of urban flood modelling, MSN_Flood's ability to simulate horizontal components of

671 water velocity is a significant advantage over simpler hydraulic models commonly used in flood modelling; the

672 complexity of urban topography (buildings, vegetation, walls, roads, embankments, ditches etc) necessitates at

673 least two-dimensional treatment of surface flows (Cook and Merwade, 2009). Spatial and temporal distribution

674 of velocity fields is also required for assessment of flood risk to people and property associated with a certain

675 flood flow magnitude. Thus, this feature will greatly benefit flood hazard management.

676 Although the modelling framework seems to be the main factor controlling accuracy of model predictions, other

677 factors such as model resolution, datasets and model parameterization also play a crucial role. In relation to

678 model topography/bathymetry, these aspects are interconnected and need to be considered jointly. Comparing

679 the 6m and 2 m grid models it can be seen that results are quite sensitive to the spatial resolution of the model.

680 The resolution acts as a filter on the model terrain so the model error increases with decreasing spatial

681 resolution, as the definition of topographic features (walls, hedges etc) are progressively lost from the model

682 bathymetry. There is a dual effect of this. Firstly, as the resolution becomes less granular the topographic

683 complexity of high density small features become sub-grid phenomena which then become parameterised

684 through roughness coefficients. Spatially varying roughness needs to be specified for different terrains, this is

685 determined based on surface classification (such as land type, vegetation or roads) within model sensitivity and

686 calibration. Secondly, the loss of larger objects such as buildings makes the model inherently ill-conditioned and

687 their loss cannot be remedied through modification of roughness coefficient alone. Errors are additionally

688 amplified by a presence of bias in the topographic data resulting from LIDAR related post-processing

689 difficulties such as representation of surface objects discussed in Mason et al. (2003).

690

691 **5 Conclusions**

692 In this research, high-resolution multi-scale modelling of coastal flooding due to tides, storm surges and rivers

693 inflows is performed. The MSN_Flood modelling system is used to simulate flood water inundation of Cork

694 City. The main findings from this research fall into two categories as follows:

695 1.   Model computational performance:

696 (a) The nesting model framework allows the model operation at practically any desired horizontal

697   resolution, including scales commensurate with resolution of LiDAR data making an optimal use of

698   such datasets. In the current setup, a four-nest cascade telescopes resolution down to the level of

699   LiDAR resolution which is sufficient to capture small scale flow features.

700 (b) The model has no limits as to the number of nesting levels and the numerical stability is maintained

701   down to the finest resolution.

702 (c) Computational effort is dictated by the number of nesting levels, the horizontal resolution of each

703   nested grid and the extents of each nested grid. Nevertheless, at the finest resolution the nested model

704   was found to be almost as accurate as a single grid model of the same resolution but at 96% saving in

705   computational cost.

706 (d) Due to its robust flooding and drying routine, the model maintains numerical stability and accuracy in

707   any part of the model domain affected by these processes.

708 (e) Internalisation of the nested boundary through a use of ghost cells combined with a tailored adaptive

709   interpolation technique permits flooding and drying of the nested boundary creating highly dynamic

710   moving boundaries. Moreover, the flooding and drying mechanism can approach the boundary of the

711   nested domain from either upstream or downstream. Nesting with a moving boundary allows

712   embedding of a child grid model within the parent model in areas where the nested boundary may wet

713   or dry. This unique feature of MSN_Flood provides a high degree of choice regarding the location of

714   the boundaries to the nested domain and therefore flexibility in model application. This capability gives

715   MSN_Flood significant advantages over other models.

716

717 2.   Model accuracy:

718 (f) The modelling system demonstrates a good capability to accurately determine physical processes at

719   different spatial scales including mesoscale coastal water circulation (90m) and small scale

720   hydrodynamics of complex urban floodplains (2m).

721   (g)   The extent of flood inundation into floodplains of Cork City and maximum water levels reached during

722   flooding were accurately simulated by the urban flood 2 m grid model.

723   (h)   Fine horizontal resolution is crucial for accurate assessment of inundation. Comparison of 6m and 2m

724   grid model RE_T in water levels shows a noticeable reduction in model performance at coarser resolution

725   over the entire domain and the error is generally greater in the dense street network of urbanized zone.

726   (i)   The urban flood model provides full characteristics of water levels and flow regimes necessary for

727   assessment of flood risk to people's safety associated with particular flood water levels and associated

728   flood water velocities.

729

730 To conclude, near-unlimited model resolution, geographically unconstrained (due to wetting and drying) nested

731 model setup, robust wetting and drying routine, computational efficiency and the capability to simulate both

732 water elevations and velocity fields, make the MSN_Flood a valuable tool for studying coastal flood inundation.

733 This research demonstrates that the adopted methodology can be successfully used in applications to coastal

734 flood modelling including complex urban environments. It can provide, at specific instances of time, accurate

735 spatial distributions of water elevations and flow magnitudes in inundated areas and can, thus, provide critical

736 information to assess possible extents of flood inundation, periods of inundation, maximum water elevations

737 reached and flood wave propagation routes and speeds. Ultimately, it can be directly used for evaluation of

738 flood risks to the area and indirectly, through some functional relationships, for risk assessment of human safety

739 and property damage. The methodology explored in this research, when applied in a forecasting sense,

740 constitutes a high resolution flood warning and planning system that can aid local decision makers targeting

741 high flood risk areas.

742

743 **Acknowledgements**

744 This publication has emanated from research conducted with the financial support of Science

745 Foundation Ireland (SFI) under Grant Numbers SFI/12/RC/2302 and SFI/14/ADV/RC3021.

746

747 **References**

748 Bates, P.D., Dawson, R.J., Hall, J.W., Horritt, M.S., Nicholls, R.J., Wicks, J., Hassan, M.A.A.M.: Simplified

749 two-dimensional numerical modelling of coastal flooding and example applications. Coastal Engineering 52,

750 795-810, 2005.

751   Bates, P.D., De Roo, A.P.J.: A simple raster-based model for flood inundation simulation. Journal of Hydrology

752   236, 54-77, 2000.

753   Bates, P.D., Horritt, M.S., Fewtrell, T.J.: A simple inertia formulation of the shallow water equations for

754   efficient two-dimensional flood inundation modelling. Journal of Hydrology 387, 33-45, 2010.

755   Brown, J.D., Spencer, T., Moeller, I.: Modeling storm surge flooding of an urban areas with particular reference

756   to modelling uncertainties; A case study of Canvey Island, United Kingdom. Water Resources research 43,

757   W06402, 2007.

758   Chen, X.: Dynamic coupling of a three-dimensional hydrodynamic mode with a latterly averaged, two-

759   dimensional hydrodynamic model. Journal of Geophysical Research 112, C07022, 2007.

760   Cook, A., Merwade, V.: Effect of topographic data, geometric configuration and modelling approach on flood

761   inundation mapping. Journal of Hydrology 377, 131-142, 2009.

762   DHI Software, 2001. Mike 21 flow model: hydrodynamic module user guide. DHI water and Environment.

763   Falconer, R.A.: A mathematical model study of the flushing characteristics of a shallow tidal bay. Proc Inst

764   Civil Eng 2 Res and Theory 77, 311-332, 1984.

765   Falconer, R.A., Chen, Y.P.: An improved representation of flooding and drying and wind stress effects in a 2-D

766   tidal numerical model. Proc Inst Civil Eng 2 res and Theory 91, 659-678, 1991.

767   Fewtreel, T.J., Duncan, A., Sampson, C.C., Neal, J.C., Bates, P.D.: Benchmarking urban flood models of

768   varying complexity and scale using high resolution terrestrial LiDAR data. Physics and Chemistry of the Earth

769   36, 281-291, 2011.

770   Formaggia, L., Gerbeau, J.F., Nobile, F., Quarteroni A.: On the coupling of 3D and 1D Navier-Stokes equations

771   for flow problems in compliant vessels. Comput Methods Appl Mech Eng 191, 561-582, 2001.

772   Gallegos, H.A., Schubert, J.E., Sanders, B.F.: Two-dimensional high-resolution modelling of urban dam-break

773   flooding: A case study of Baldwin Hill, California. Advances in Water Resources 32, 1323-1335, 2009.

774   Gomes-Pereira, L.M., Wicherson, R.J.: Suitability of laser data for deriving geographical data: a case study in

775   the context of management of fluvial zones. Photogrammetry and Remote Sensing 54, 105-114, 1999.

776   Haidvogel, D.B., H. Arango, W.P. Budgell, B.D. Cornuelle, E. Curchitser, E. Di Lorenzo, K. Fennel, W.R.

777   Geyer, A.J. Hermann, L. Lanerolle, J. Levin, J.C. McWilliams, A.J. Miller, A.M. Moore, T.M. Powell, A.F.

778   Shchepetkin, C.R. Sherwood, R.P. Signell, J.C. Warner, J. Wilkin: Ocean forecasting in terrain-following

779   coordinates: Formulation and skill assessment of the Regional Ocean Modeling System. J. Comp. Phys. 227(7),

780   3595-3624, 2008.

781   Halcrow: Lee catchment flood risk assessment and management study. Hydrology report. Halcrow Group

782   Ireland Ltd. , 2008.

783   Holt, J., Harle, K, Proctor, R., Michel, S., Ashworth, M., Batstone, C., Allem, I., Holems, R., Smyth T., Haines,

784   K., Bretherton, D., Smith G.: Modelling the global coastal ocean. Philos Trans Soc A 367, 939-951, 2009.

785   Horritt, M.S.: Calibration and validation of a 2-dimensional finite element flood flow model using satellite radar

786   imaginary. Water Resources Research 36, 3279-3291, 2000.

787   Horritt, M.S., Bates, P.D., Mattinson, M.J.: Effects of mesh resolution and topographic representation in 2D

788   finite volume models of shallow water fluvial flow. Journal of Hydrology 329, 306-314, 2006.

789   Hunter, N.M., Bates, P.D., Neelz, S., Pender, G., Villanueva, I., Wright, N.G., Liang, D., Falconer, R.A., Lin,

790   B., Waller, S., Crossley, A.J., Mason, D.C.: Benchmarking 2D hydraulic models for urban flooding. Water

791   Management 161, 13-30, 2008.

792   Kashefipour, S.M., Lin, B., Harris, E., Falconer, R.A.: Hydro-environmental modelling for bathing water

793   compliance of an estuarine basin. Water Research 36, 1854-1868, 2002.

794   Korres, G., Lascaratos, A.: A one-way nested eddy resolving model of the Aegean and Levantine Basins:

795   implementation and climatological runs. Ann Geophys 21, 205-220, 2003.

796   Kvočka, D., Falconer, R.A., Bray, M. : Appropriate model use for predicting elevations and inundation extent

797   for extreme flood events. Natural Hazards 79, 1791-1808, 2015.

798   Lin, B., Falconer, R.A.: Tidal flow and transport modelling using ULTIMATE QUICKEST scheme. Journal of

799   hydraulic Engineering 123, 303-314, 1997

800   McMillian, H.K., Brasington, J.: Reduced complexity strategies for modelling urban floodplan inundation.

801   Geomorphology 90, 226-243, 2007.

802   Mark, O., Weesakul, S., Apirumanekul, C., Aroonnet S.B., Djordjevic, S.: Potentials and limitations of 1D

803   modelling of urban flooding. Journal of Hydrology 299, 284-299, 2004.

804   Marks, K., Bates, P.D.: Integration of high-resolution topographic data with floodplain flow models.

805   Hydrological processes 14, 2109-2122, 2000.

806   Mason, D.C., Cobby, D.M., Horritt, M.S., Bates, P.D.: Floodplain friction parameterization in two-dimensional

807   river flood models using vegetation heights derived from airborne scanning altimetry. |Hydrological Processes

808   17, 1711-1732, 2003.

809   Mason, D.C., Horrit, M.S., Hunter, N.M., Bates, P.D.: Use of fused airborne scanning laser altimetry and digital

810   map data for urban flood modelling. Hydrological Process 21, 1436-1447, 2007.

811   Nash, S.: Development of an adaptive mesh inter-tidal circulation model. PhD Thesis Collage of Engineering

812   and Informatics, National University of Ireland, Galway, 2010.

813   Nash, S., Hartnett, M.: nested circulation modelling of inter-tidal zones: details of nesting approach

814   incorporating moving boundary. Ocean Dynamics 60, 1479-1495, 2010.

815   Nash, S, Hartnett, M..: Development of a nested circulation model: boundary error reduction. Environmental

816   Modelling and Software 53, 65-80, 2014.

817   Nittis, K., Perivoliotis, L., Korrea G., Tziavos, C., Thanos, I.: Operational monitoring and forecasting for marine

818   environmental applications in the Aegean sea. Environ Modell Softw 21, 243-257, 2006.

819   Olbert A.I., Hartnett M.: Storms and surges in Irish coastal waters. Ocean Modelling 34, 50–62, 2010.

820   Pappenberger, F., Beven, K., Horritt, M., Blazkova, S.: Uncertainty in the calibration of effective roughness

821   parameters in HEC-RAS using inundation and downstream level observations. Journal of Hydrology 302, 46-

822   69, 2005.

823   Pender, G., Neelz, S.: Benchmarking of 2D hydraulic modelling packages. SC080035/R2 Environmental

824   Agency, Bristol, p. 169, 2010.

825   Ponte, R.M.: Understanding the relation between wind- and pressure-driven sea level variability. Journal of

826   Geophysical Research 99, 8033-8039, 1994.

827   Robins, P.E., Davies, A.G., Jones, R.:Application of coastal model to simulate present and future inundation and

828   aid coastal management. J Coast Conserv 15, 1-14, 2011.

829   Sanders, B.F., Schubert, J.E., Detwiler, R.L.: ParBreZo: A parallel, unstructured grid, Godunov-type, Shallow

830   water code for high-resolution flood inundation modelling at the regional scale. Advances in Water Resources

831   33, 1456-1467, 2010.

832   Simmons A.J., Burridge D.M., Jarraud M., Girard C., Wergen W.: The ECMWF medium-range prediction

833   models development of the numerical formulations and the impact of increased resolution. Meteorol Atmos

834   Phys 40, 28-6, 1989.

835   Smith, L.C.: Emerging applications of interferometric synthetic aperture radar (INSAR) in geomorphology and

836   hydrology. Annals Assoc Am Geography 92, 385-398, 2002.

837   Uppala, S.M., Kallberg, P.M., Simmons, A.J., Andrae, U., Bechtold, V., Fiorino, M., Gibson, J., Haseler, J.,

838   Hernandez, A., Kelly, G., Li X., Onogi, K., Saarinen, S., Sokka, N., Allan, R., Andersson, E., Arpe, K.,

839   Balmaseda, M., Beljaars, A., Berg, L., Bidlot, J., Bormann, N., Caires, S., Dethof, A., Dragosavac, M., Fisher,

840   M., Fuentes, M., Hagemann, S., Holm, E., Hoskins, B., Isaksen, L., Janssen, P., McNally, A., Mahfouf, J.,

841   Jenne, R., Morcrette, J., Rayner, N., Saunders, R., Simon, P., Sterl, A., Trenberth, K., Untch, A., Vasiljevic ,D.,

842   Viterbo, P., Woollen, J.: The ERA-40 reanalysis. Quart J Roy Meteorol Soc 131, 2961-3012, 2005.

843   Yang, Z., Wang, T., Khangaonkar, T., Breithaupt, S.: Integrated modelling of flood flows and tidal

844   hydrodynamics over coastal floodplains. Environmental Fluid Mechanics 12, 63-80, 2012.

845   Yu, D., Lane, S.N.: Urban fluvial flood modelling using two-dimensional diffusion-wave treatment: 1. Mesh

846   resolution effects. Hydrological Processes 20, 1541-1565, 2006.

847

848

849

850

851

852

853

854

855

856

857

858

859

860

861

862

863

864

865

866

867

868

869

870   Tables

871

872   Table 1. Configuration of nested models

Model	Grid size m	Timestep s	Parent model	Parent-to-model grid ratio
Parent grid (PG90)	90	18	--	1:1
Single grid (SG30)	30	6	PG90	1:1
Child grid 1 (CG30)	30	6	PG90	3:1
Child grid 2 (CG06)	6	0.6	CG30	5:1
Child grid 3 (CG02)	2	0.2	CG06	3:1
Single grid (SG02)	2	0.2	CG06	1:1

873

874

875   Table 2. Summary of error analyses for PG90 and CG30 models within CG30 model area.

Error Analyses Parameter	SG30	
	PG90	**CG30**
Water Elevation:		
- RE_D [%]	5.9	1.1
- AE_D [x10^{-2} m]	8.0	1.2
- $RE_T > 1\%$ [%]	94	28
Current Velocity:		
- RE_D [%]	22.4	0.5
- AE_D [x10^{-3} m/s]	2.70	0.13
- $RE_T > 5\%$ [%]	72	4

876

877

878

879   Table 3. Error statistics of water elevations simulated by the CG06 model and measured at Tivoli tidal gauge

880   station. Heights are in meters

Code	COR	NSD	RMSD	RMSE	RMSdiff
CG06_1	0.992	1.021	0.141	0.142	0.022
CG06_2	0.996	1.023	0.104	0.106	0.024
CG06_3	0.995	1.084	0.075	0.075	0.020

881

882

883   Table 4. Error statistics of water elevations at four locations simulated by the CG06 and CG02 models. Heights

884   are in meters

Code	COR	NSD	RMSD	RMSE	RMSdiff
CG02_1	0.995	1.033	0.080	0.111	-0.081
CG02_2	0.997	1.014	0.109	0.195	-0.181
CG02_3	0.998	1.045	0.056	0.076	-0.064
CG02_4	0.999	0.999	0.006	0.006	0.000

885

886

887

888

889

890

891

892

893

894

895

896

897
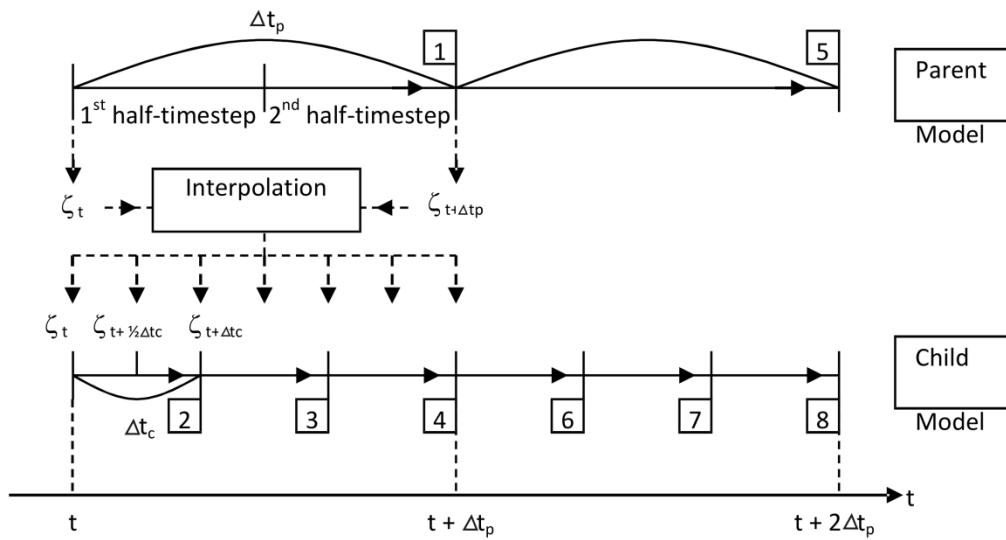
898

899

900   Figure 1: The nesting procedure for a single level of nesting and one variable only - water surface elevation, ζ.

901
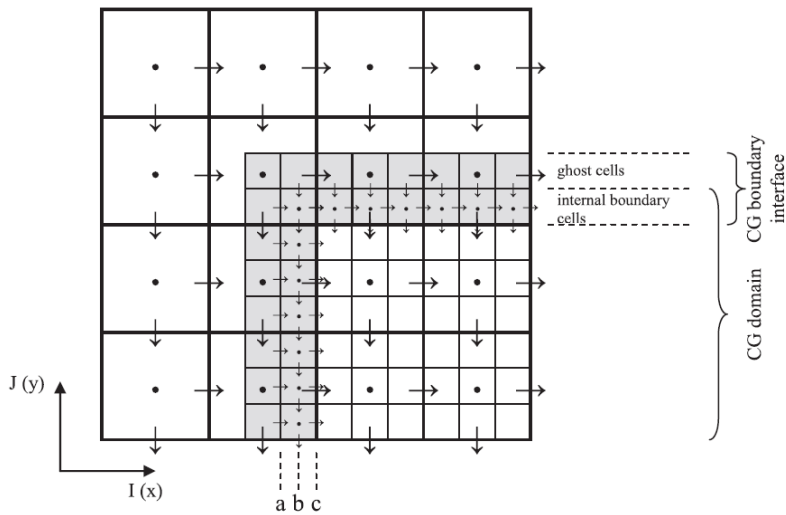
902

903   Figure 2: Schematic illustration of the internal boundary configuration for 3:1 nesting ratio.

904

905
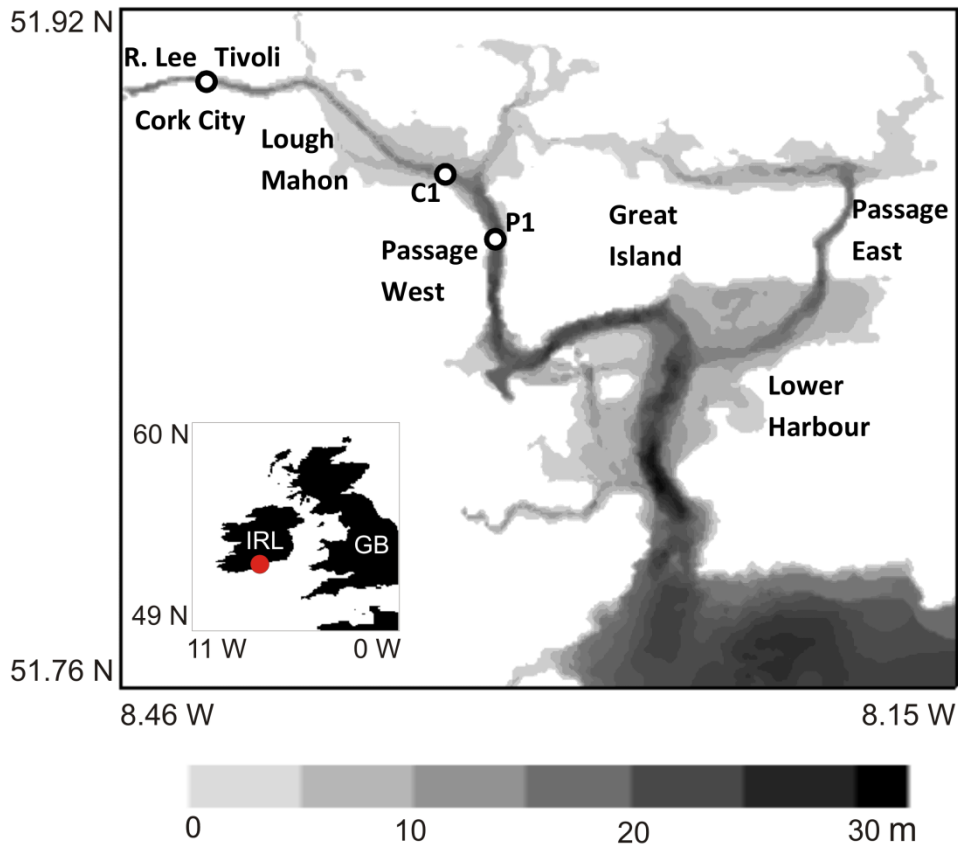
906

907   Figure 3: Bathymetry of Cork Harbour (m) with selected locations. Red dot denotes location of Cork Harbour

908   on the cost of Ireland.
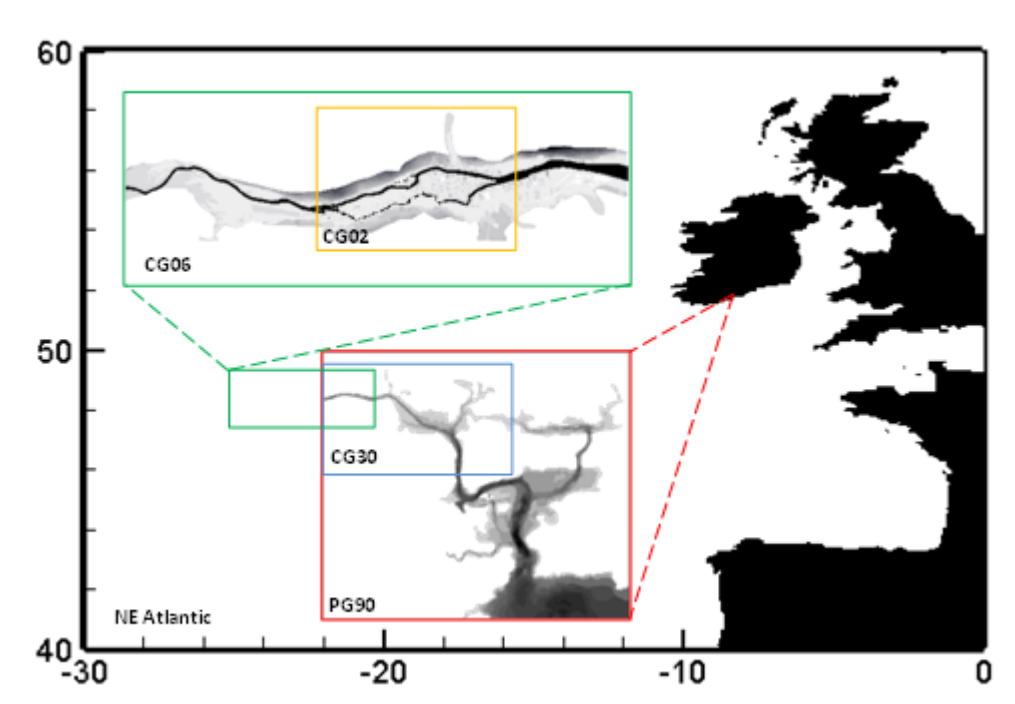
909

910   Figure 4: Four-level nesting structure of Cork Harbour and City nested model.

911
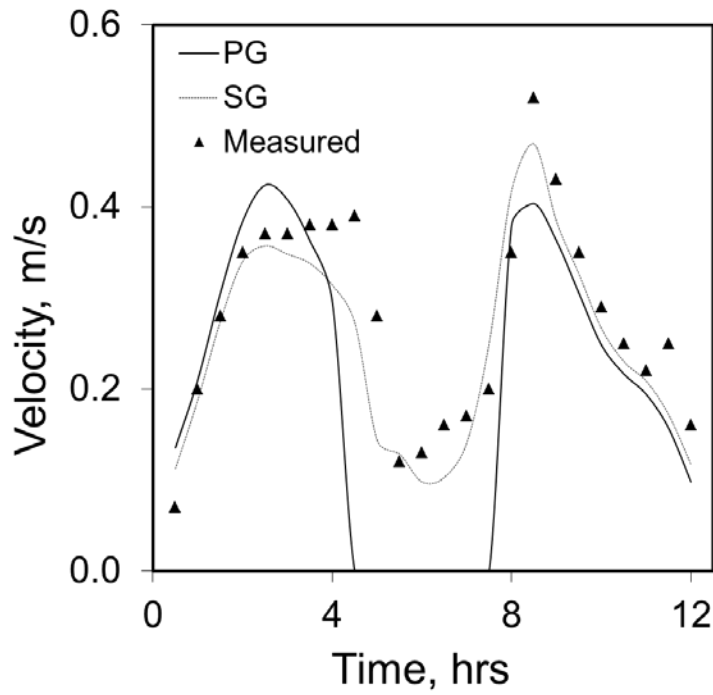
912

913   Figure 5: Comparison of computed and measured velocities at Passage West (point C1 in Figure 3).

914
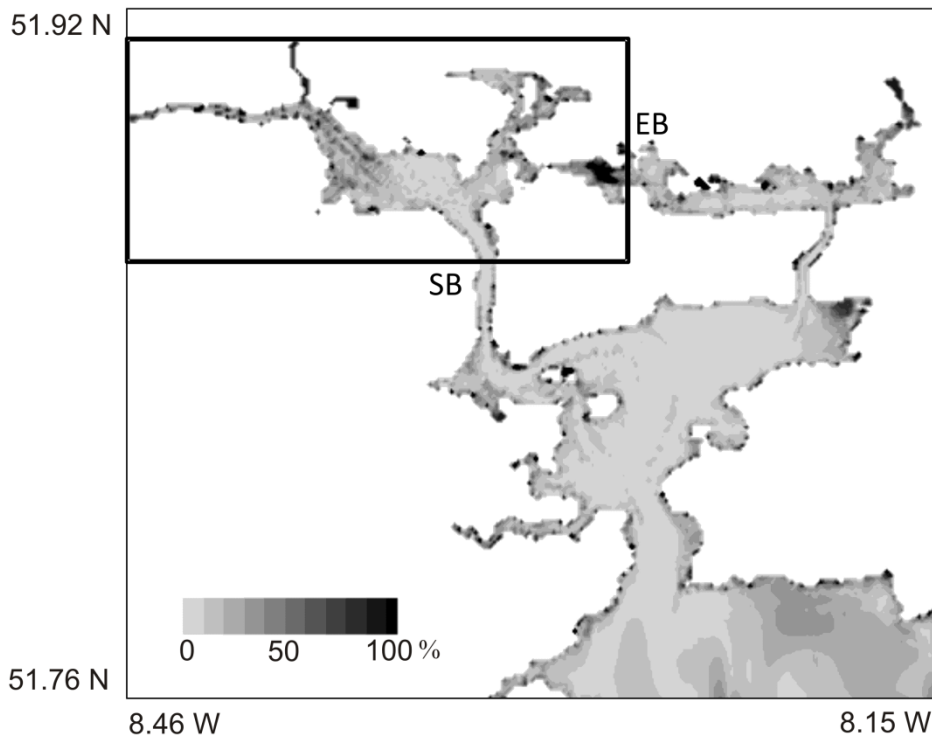
915

916   Figure 6: RE_T (%) in PG90 velocities. Black box shows extents of CG30 model and locations of nested

917   boundaries. EB - east boundary, SB – south boundary.

918 (a) (b)
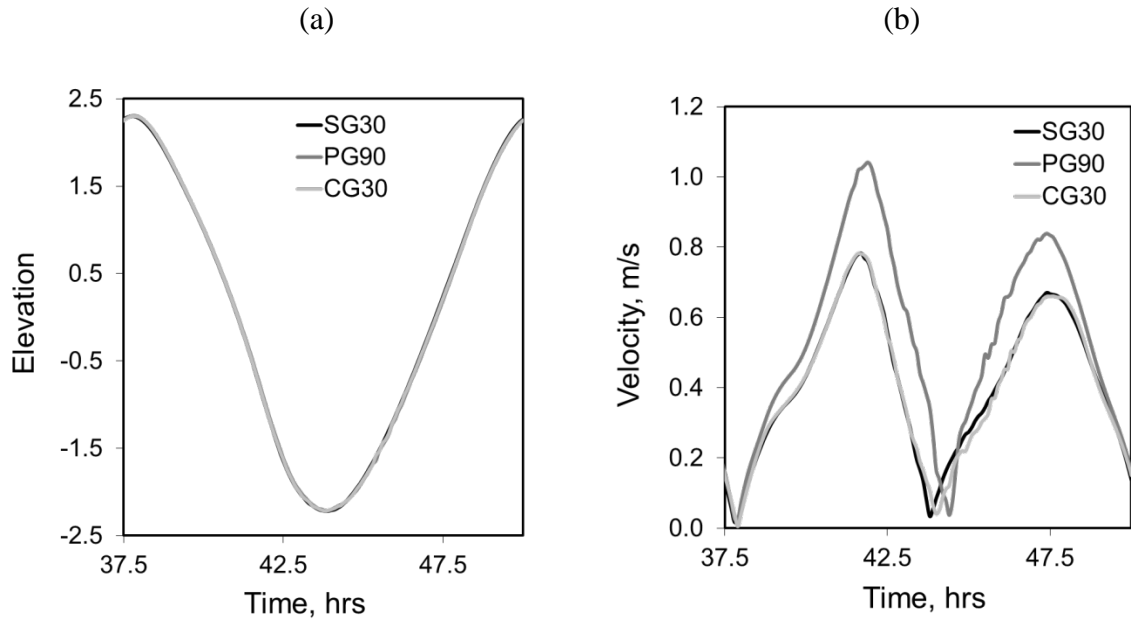
919

920

921 Figure7: Comparison of (a) water elevations and (b) current velocities at point C1 in Lough Mahon.

922
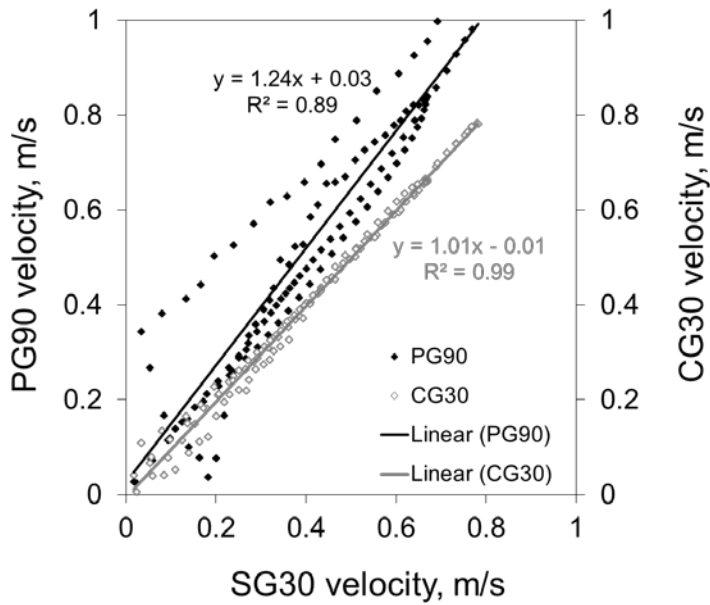
923

924 Figure 8: Comparison of modelled velocities for various grid setups at point C1 in Lough Mahon. Time series

925 data are overlain by a linear trend.

926

927 (a) (b)
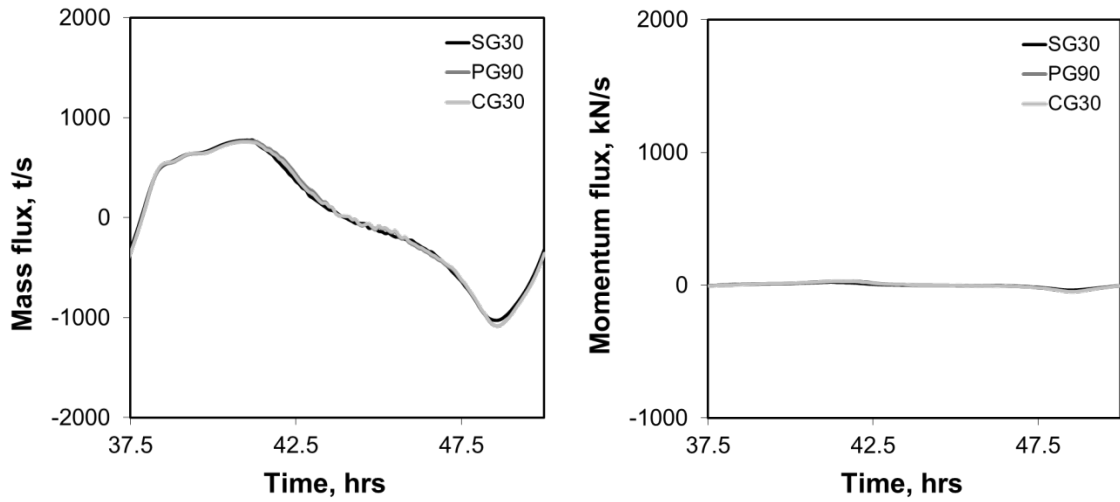
928

929 Figure 9: Comparison of (a) mass and (b) momentum fluxes across EB boundary; PG90 and CG30 timeseries

930 are coincident.

931

932   (a)   (b)
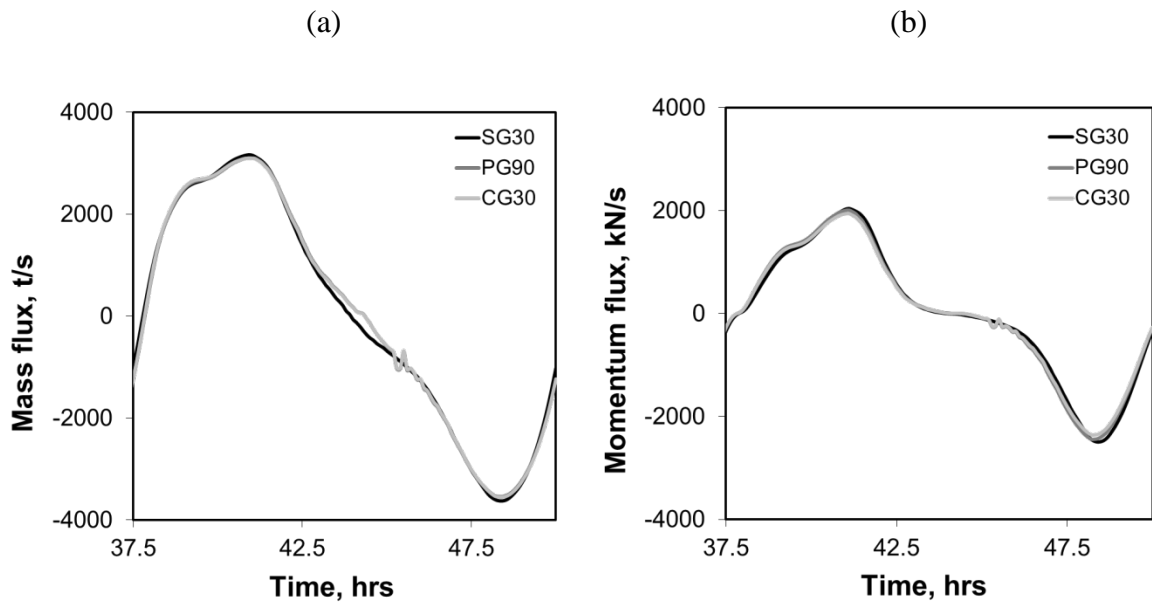
933

934 Figure 10: Comparison of (a) mass and (b) momentum fluxes across SB boundary; PG90 and CG30 timeseries

935 are coincident.

936
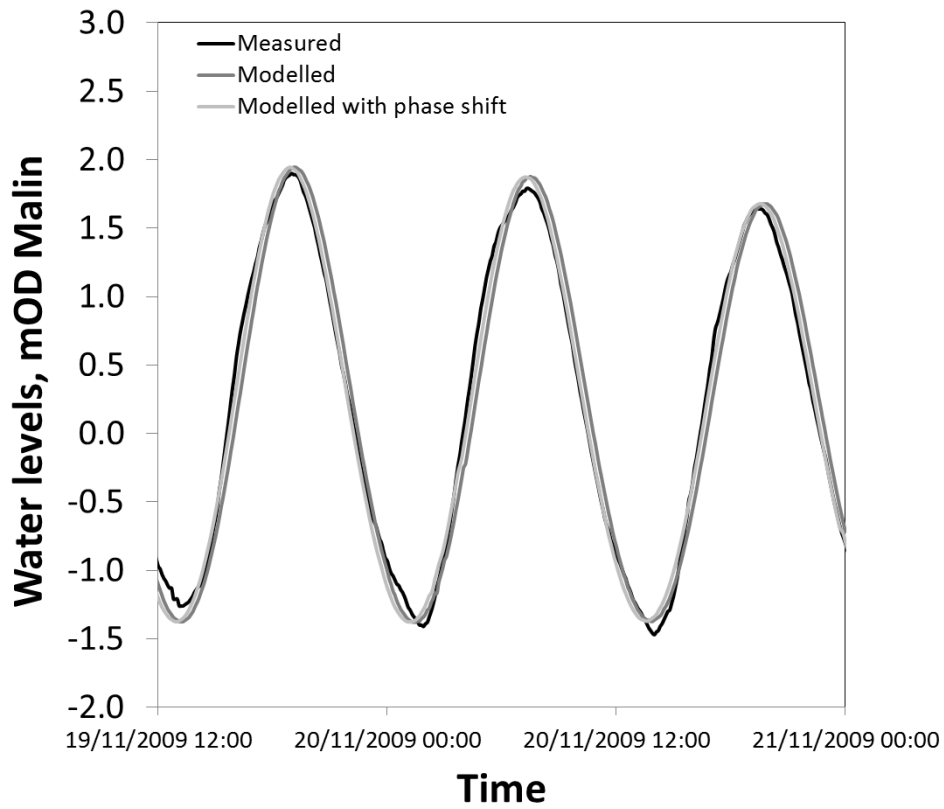
937

938   Figure 11: Water elevations predicted by the CG06 model and measured at Tivoli tidal gauge station.

939
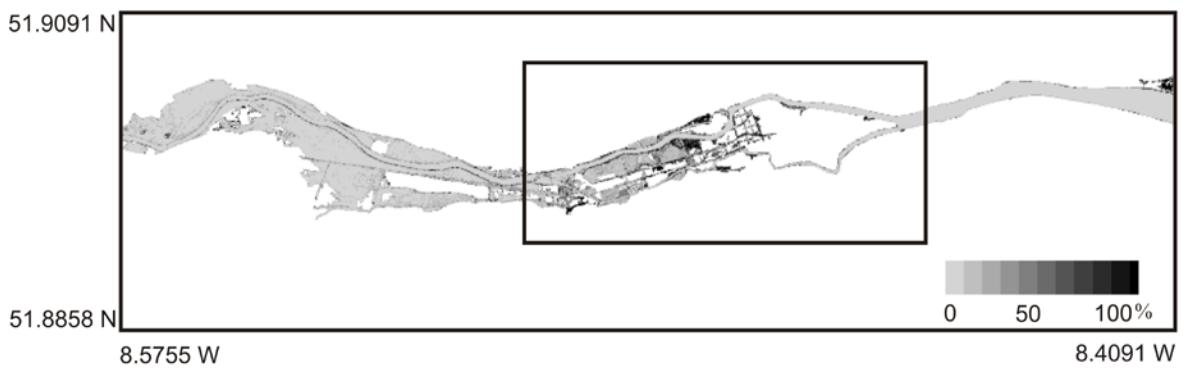
940

941   Figure 12: Water level RE_T (%) in CG06 relative to SG02 . Black box shows extents of CG02 model and

942   locations of nested boundaries.

943

944

945

946

(a) (b)

(c) (d)
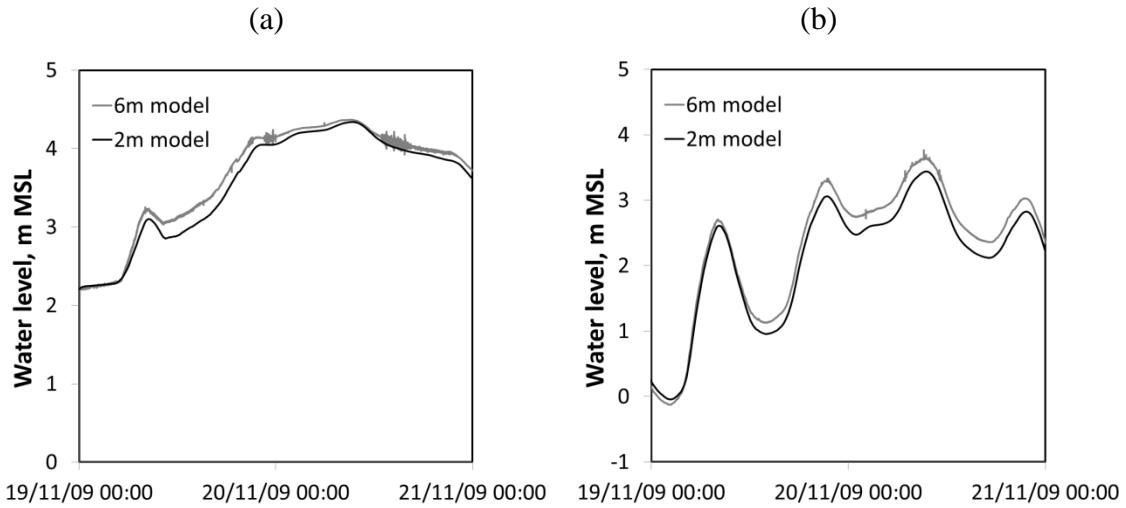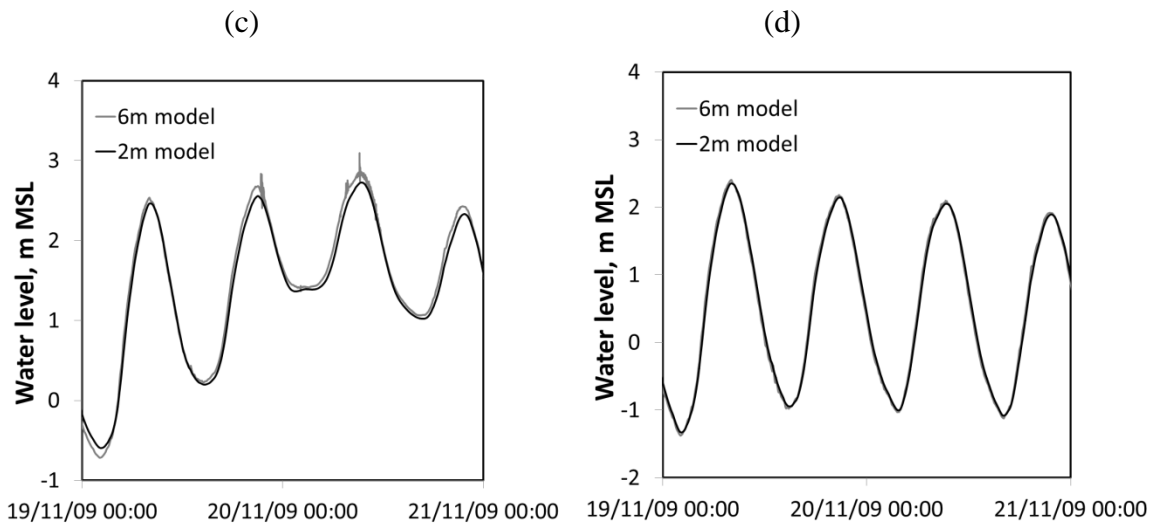
Figure 13: Timeseries of water elevations predicted by CG06 and CG02 models at four locations (a) CG02_1, (b) CG02_2, (c) CG02_3, (d) CG02_4.
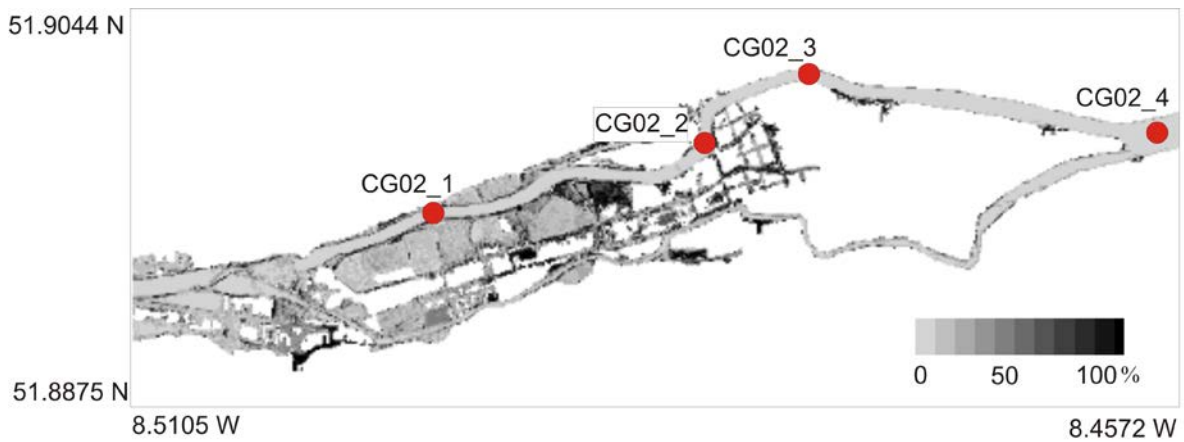
Figure 14: Water level RE_T (%) in CG02 relative to SG02 . Red dots denotes points used in water level analysis (see Figure 13).
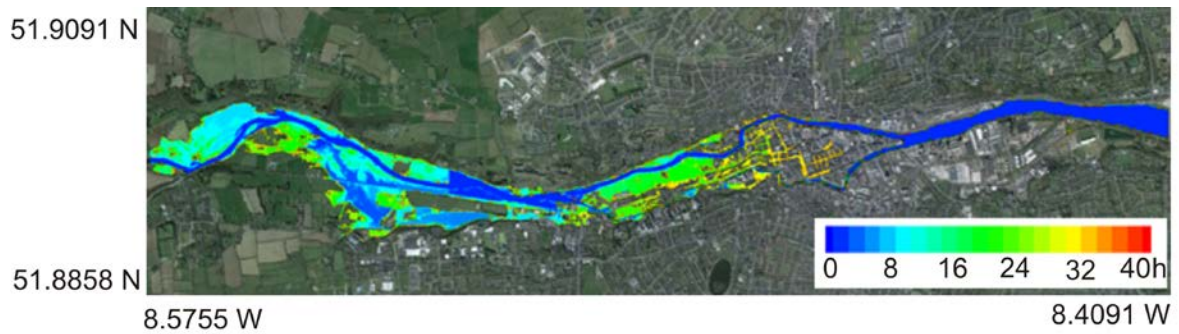
956

957 Figure 15: Temporal evolution of flood wave through upper and lower floodplain of Cork City during

958 November 2009 flood event modelled by CGO6; contours represent 2-hour intervals.

959

960

961 Figure 16: Maps of flood inundation observed by (a) OPW and (b) modelled (contours represent 2-hour

962 intervals). Evolution of modelled flood wave is a combined output of CG06 and CG02 models.

963

964
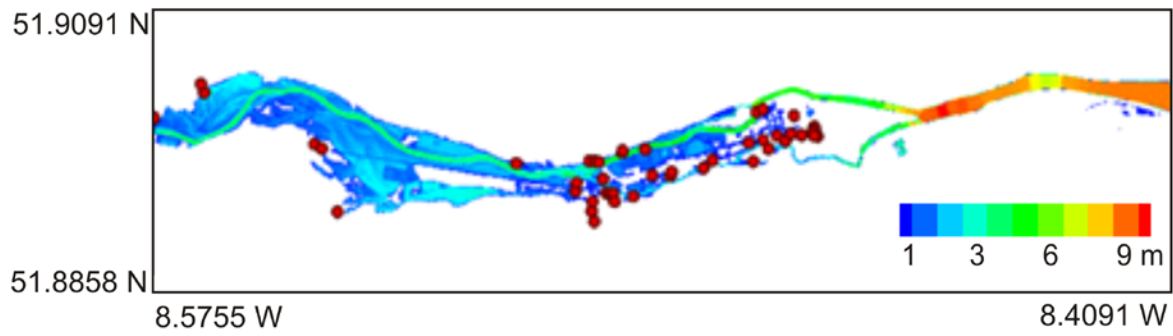
965

966 Figure 17: Maximum water levels during November 2009 flood event and water level survey points marked as

967 red dots.

968

969
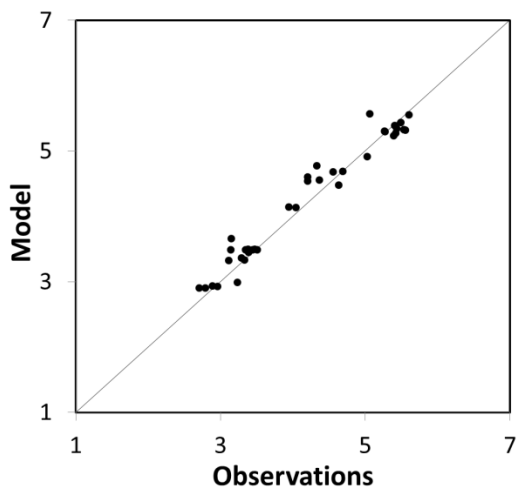
970

971 Figure 18: Comparison of modelled and observed maximum water elevations at 38 stations.

972
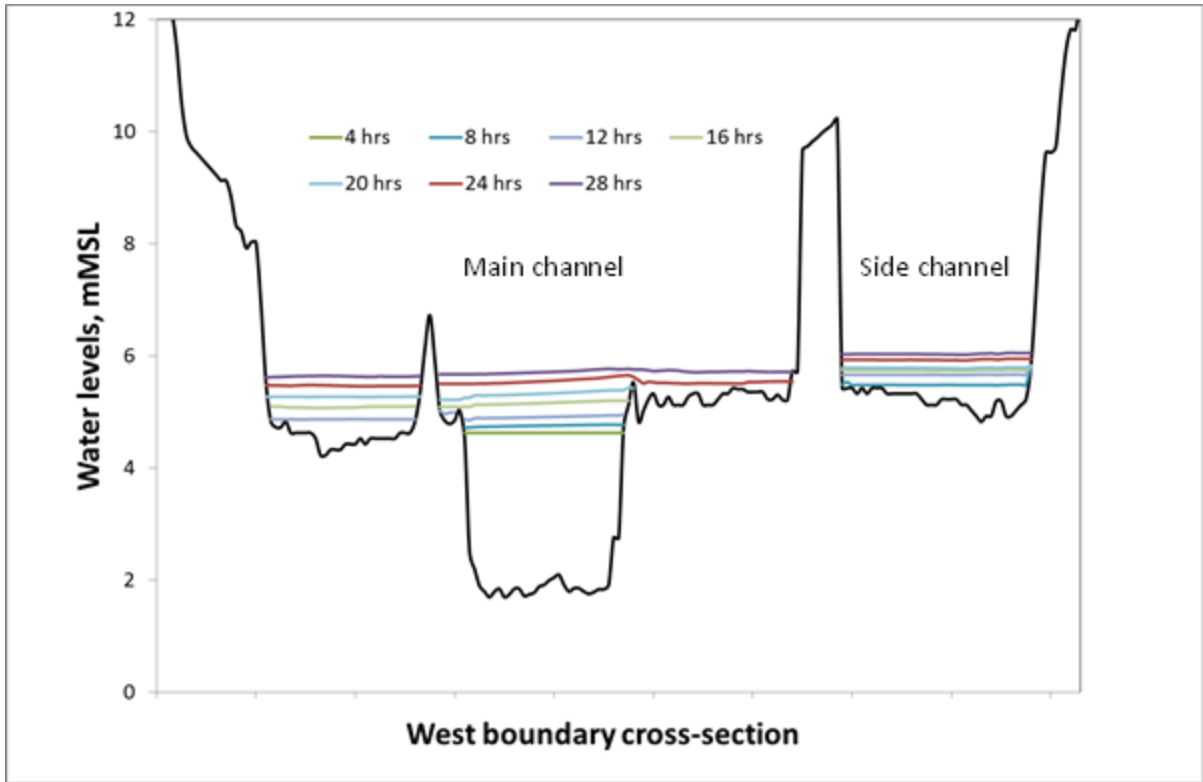
973

974   Figure 19: Cross section through west boundary of CG02 model with water elevation marks for selected time

975   points.

976
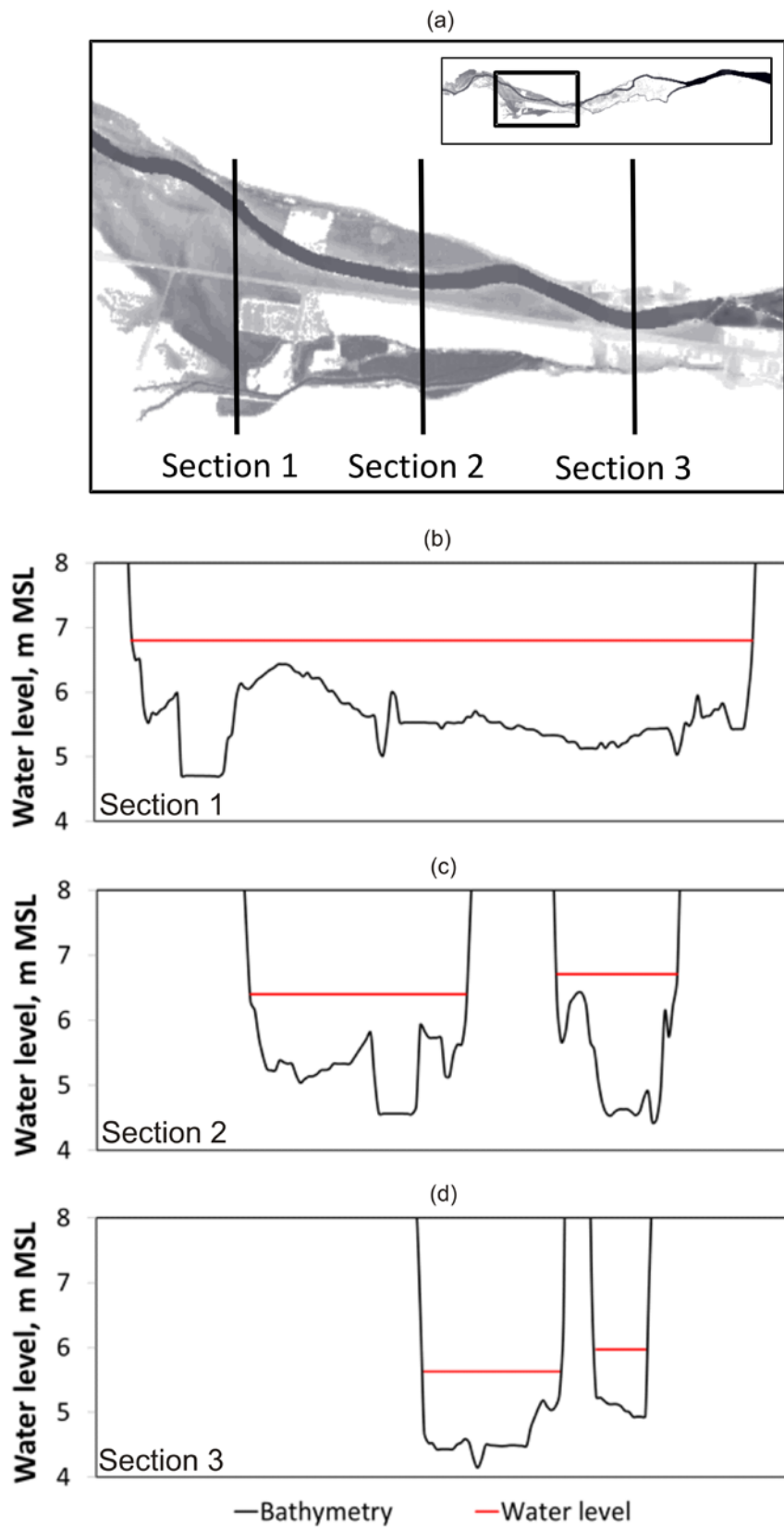
977

978 Figure 20: (a) Flood extent and (a-c) water elevations at three cross-sections during flooding simulated by

979 CG06.

980

981
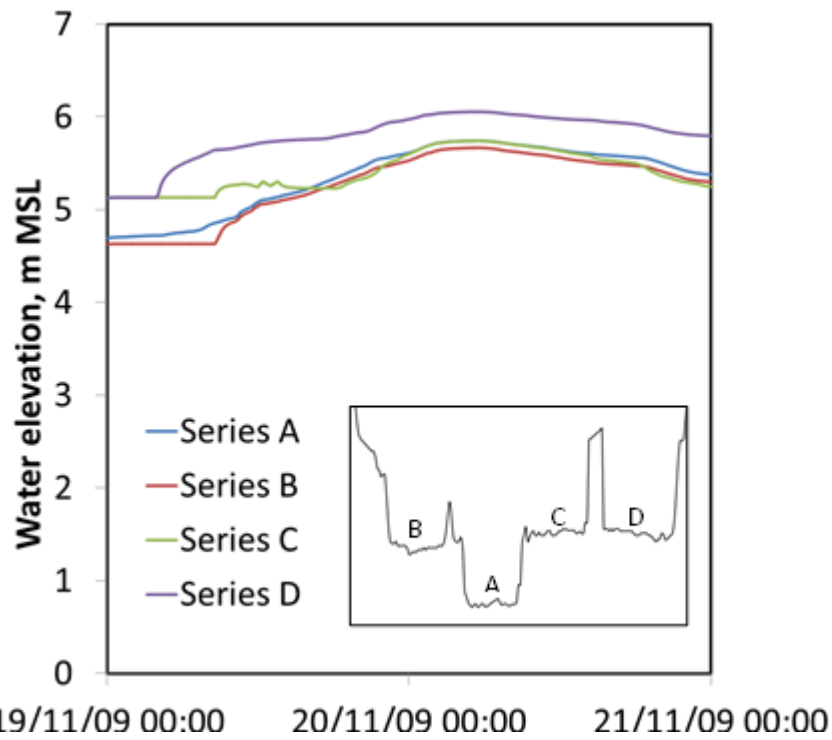
982 Figure 21: Timeseries of water elevations across the western nested boundary of CG02.

983

984

985
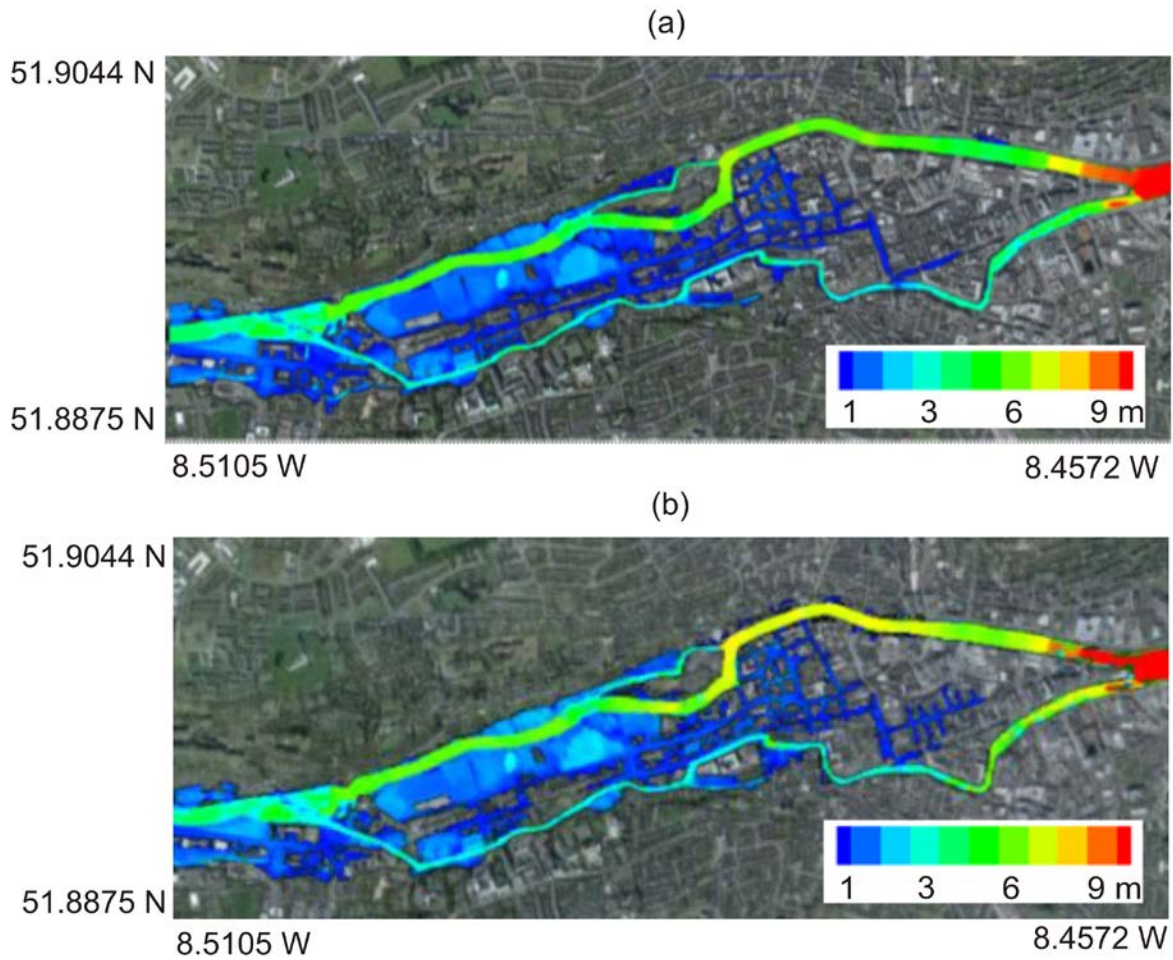
986 Figure 22: Comparison of flood extent simulated by (a) CG02 and (b) CG06 models. Contours represent water

987 levels (m).

988
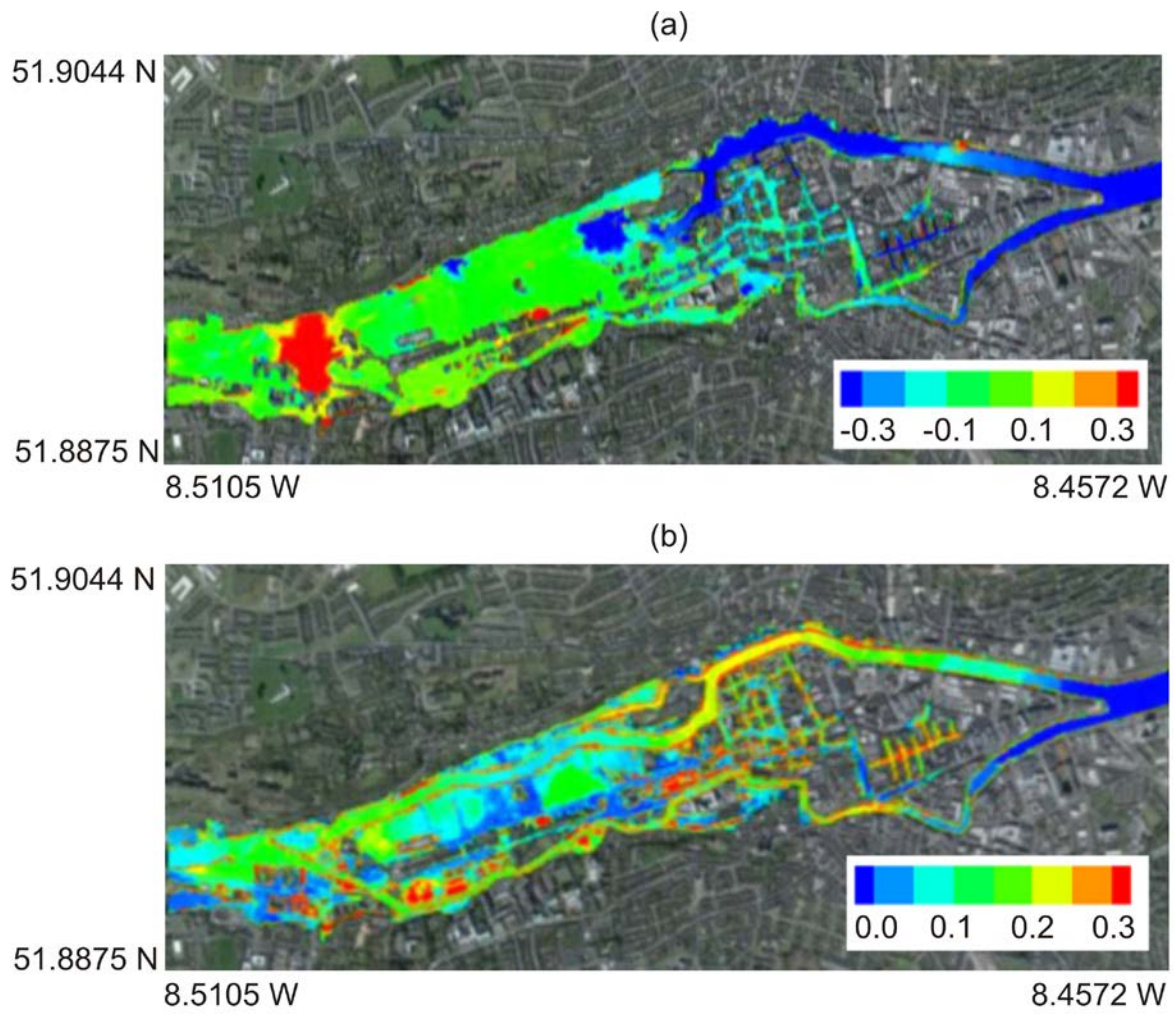
989

990 Figure 23: (a) Difference in water elevations (m) between CG06 and CG02 models and (b) RMSE contour plot

991 over time.

992

993

994

995

996

997

998

999 (a)   (b)
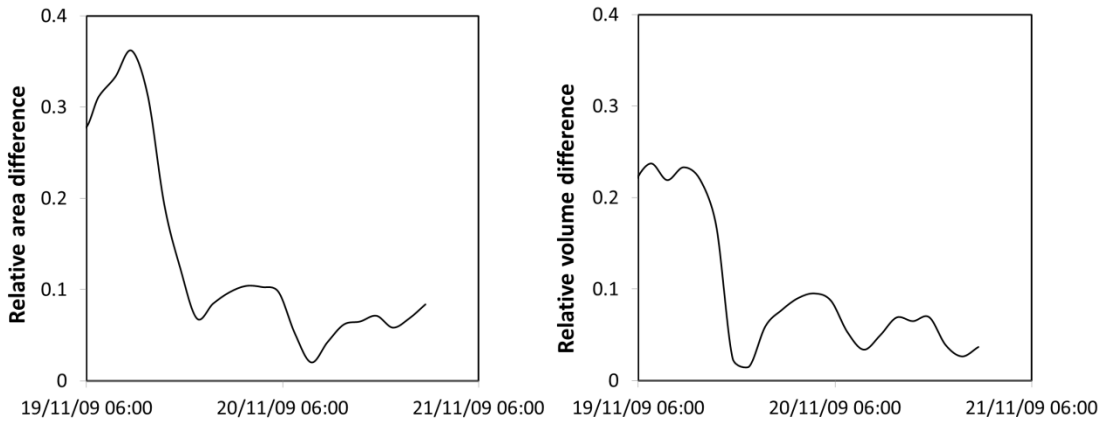
1000

1001

1002   Figure 24: Evolution of the relative difference in (a) total area of inundation and (b) volume of water in

1003   inundated area between CG06 and CG02 models. See text for explanation of relative difference.

1004
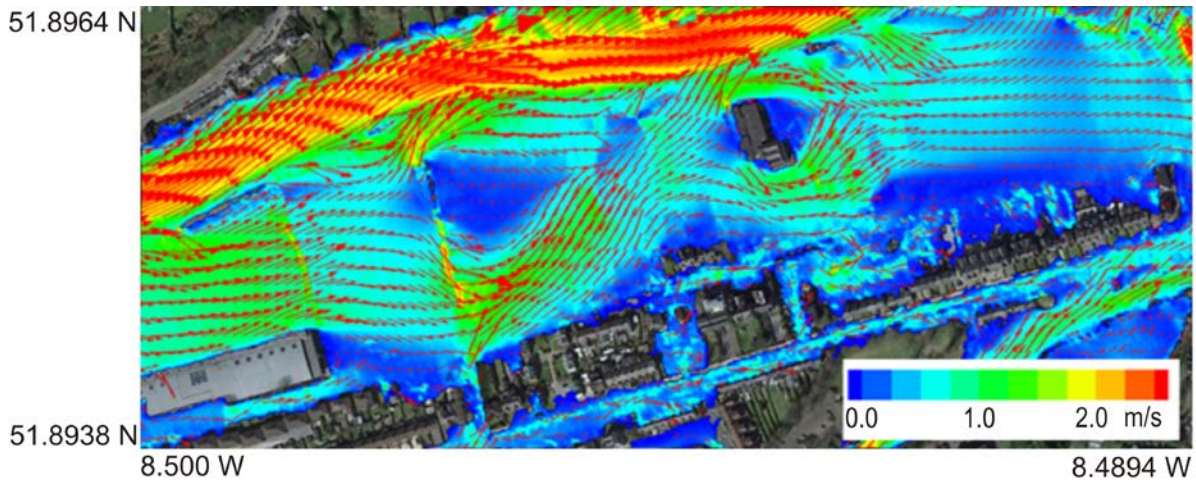
1005

1006   Figure 25: Map of velocity contours (m/s) with vectors showing magnitude and direction of velocities in the

1007   downstream floodplains of Cork City.

1008

1009

1010

1011